INVESTIGATION ON STRUCTURAL AND ELECTROCHEMICAL PROPERTIES OF La_2CoMnO_6 DOUBLE PEROVSKITE FOR ENERGY STORAGE APPLICATIONS

Project report submitted to the

University of Kerala

In partial fulfillment of the requirements for the award of the degree of

MASTER OF SCIENCE IN PHYSICS

2020-2022

ABSTRACT

Double perovskites oxides possess unique properties for energy storage applications due to their more orderly arrangement of structures than the doped perovskites, thus controlling the distortion in lattice and thereby increasing cyclic stability. Recently, due to this high energy demand, La_2CoMnO_6 perovskite manganite was explored as a suitable electrode material for high-performance supercapacitors. La_2CoMnO_6 double perovskite was synthesized via modified combustion route. XRD with Rietveld refinement confirms monoclinic structure with space group of $P2_1/n$. Irregular shaped porous morphology and elemental analysis were determined from FE-SEM and EDAX spectra respectively. Existence of mixed valence state of Co and Mn were verified by XPS spectra and its bandgap was determined using Tauc plot. Vibrational analysis validates the formation of perovskite phase and degeneracy in Raman modes/thermal broadening provides signature vibrational bands corresponding to stretching and bending motions of MnO_6 and CoO_6. Supercapacitor performance using La_2CoMnO_6 as electrode material exhibits 84% of cyclic stability after 500 cycles. This findings confirmed that La_2CoMnO_6 manganite can be used for energy storage applications.

CONTENTS

List of figures

List of tables

CHAPTER 1

INTRODUCTION TO SUPERCAPACITORS

1.1 Introduction

Due to the global energy crisis, the ever-increasing need for energy and environmental concerns have led to the investigation of novel, eco-friendly, efficient, high-performance, and cost-effective energy storage systems [1-3]. To address these issues, significant research efforts have been made to develop devices with a variety of benefits, including high efficiency, sustainability, environmental friendliness, and long service life [4,5]. Electrical energy must be created from renewable sources and stored efficiently using improved storage technologies in the future [5]. Unconventional energy storage devices, such as batteries, fuel cells, and supercapacitors, can meet the requirement for efficient energy storage while also being environmentally friendly. Technology development for harvesting and converting sustainable energies to power that may be used for electronics has been the subject of extensive investigation. However, because to the intermittent nature, unequal regional distribution, and unpredictability of natural availability of these sustainable energy resources, reliable and efficient energy storage technology is essential for full utilisation of these resources. Supercapacitors are energy storage devices that fall between between batteries and capacitors. While retaining a clean and safe technique of storing electric energy, supercapacitors provide better power densities, longer life cycles, and shorter charge/discharge time intervals [6].

Researchers are paying attention to these storage solutions right now. Efficient electrical storage devices, such as batteries and supercapacitors (SC), are viable prospects for addressing future demand for electric propulsion systems. Supercapacitors are a type of capacitor that sits between batteries and traditional capacitors. Scientists have been studying how electric charge is stored at the interface between an electrode (metal) and an electrolyte for decades. Batteries, fuel cells, and supercapacitors (SC) or ultra-capacitors are electrochemical energy conversion systems that are utilised as storage devices in a variety of modern applications. In use, these are the most effective

and practical. SC has gained widespread attention because it may be able to bridge the power-energy gap between batteries and traditional capacitors. In a wide range of electronic and engineering applications, SCs are required. These applications primarily require a rapid pulse of high energy, such as the surge of energy required to start hybrid electric and fuel cell vehicles. Regular batteries are unable to give such a significant amount of energy in such a short period of time. Electronics, home appliances, renewable energy (wind turbines), and mechanical regenerative power tools all use SC.

1.2 Principal and Mechanism of Energy Storage in Supercapacitors

Energy is stored in supercapacitors through a charging and discharging process at the electrode-electrolyte interface[7-9]. The energy storage principle of a supercapacitor is almost identical to that of a regular capacitor. The primary distinguishing feature is the ability to quickly release and store energy. The specific capacitance of a supercapacitor is increased due to porous electrodes with a higher surface area. A supercapacitor's specific capacitance can vary from a few hundred to a few thousand times that of a typical capacitor. The storage capacity of normal capacitors is measured in microfarads or millifarads, whereas that of a supercapacitor is measured in hundreds of farads. Another distinguishing aspect is the device's equivalent series resistance, which is much lower in a supercapacitor than in a regular capacitor.

The following is the concept that governs energy storage:

- Charge adsorption near the electrode-electrolyte interface, which results in a higher specific capacitance.
- Pseudo capacitance caused by surface redox processes that are proportional to the potential.

In supercapacitor, charge storage is mostly a surface phenomenon. In a supercapacitor, charge is held both electrochemically and electrostatically. Due to the wide interfacial area of the electrodes and a charge/discharge mechanism similar to that of a typical capacitor, a supercapacitor can store more energy based on the electric double layer principle. Aside from that, extra capacitance is created as a result of charge separation at the electrode-electrolyte interface. Pseudo Capacitance is a result of faradaic charge shift of reversible redox reactions, rather than the intercalation and de-intercalation processes used in batteries.

Both types of capacitor materials are mixed in an electrochemical energy storage device to get the benefits of both capacitive materials. The energy and power density of a hybrid energy storage device can be higher than that of a pseudocapacitive or electric double layer capacitor (EDLC) material alone. When compared to batteries, supercapacitors have a higher power density, but their energy density is still substantially lower.

Figure 1.1 shows a schematic illustration of a supercapacitor. Two electrodes, electrolyte solution, separator, and current collector are the essential components of the supercapacitor assembly. Each of these components has an impact on the performance of a supercapacitor.

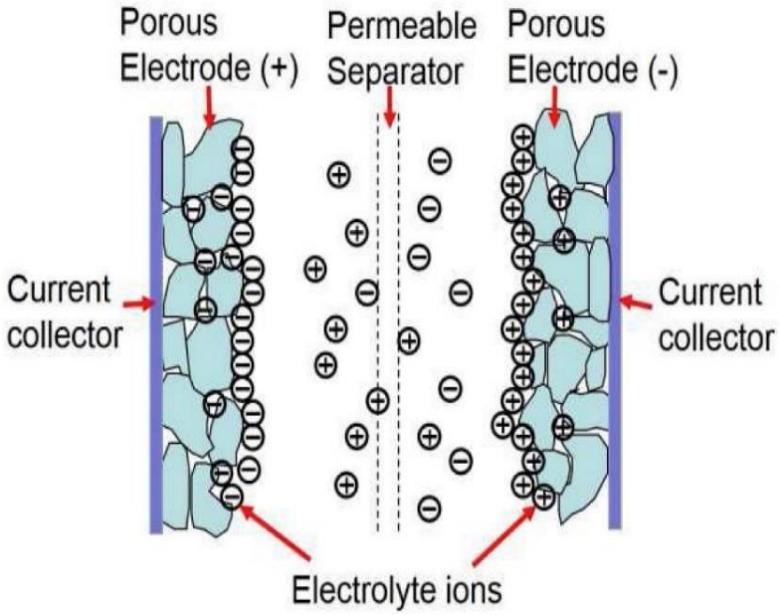

Figure. 1.1. Schematic layout of supercapacitor.

The importance of SC can be seen using the "Ragone Plot" of specific energy and power density, as shown in Figure 1.2. The Ragone figure, shown in Figure 1.2 , compares the energy and power density of supercapacitors with other batteries [1]. Supercapacitors differ from batteries in that they have an ultrahigh power density, which allows them to be charged and drained in seconds. As a result, supercapacitors are utilised in applications that require high power uptake or delivery as well as pulsed energy, such as stop-and-go systems,

industrial energy management systems, and electric cars (which are typically used in conjunction with lithium-ion batteries) [2,3].

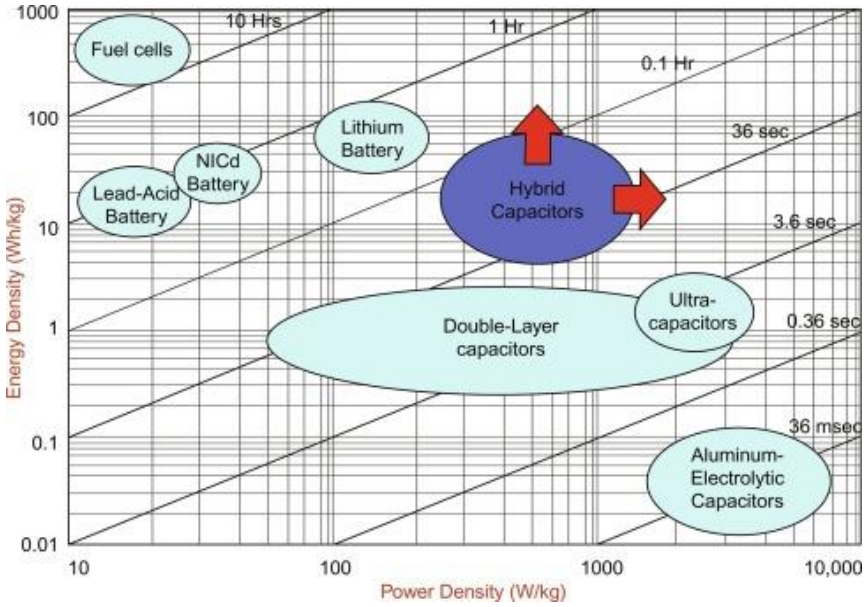

Figure 1.2: Ragone chart showing energy density as a function of power density of various capacitors and batteries.

1.3 Classification Of Supercapacitors

Supercapacitors can be divided into following categories

- Electric double-layer capacitors (EDLC, non-Faradic capacitors)
- Pseudocapacitors (Faradic capacitors)

  and third one is called hybrid SC in which one electrode exhibits double layer and other exhibits pseudocapacitive properties (see fig. 1.3).

SCs can use both electrode-based and non-electrode-based energy storage techniques. Charges electrostatically deposit within the porous structures of electrodes in EDLCs, which are mostly comprised of carbonaceous materials. Pseudocapacitive SCs, which are mostly constructed of transitional metal oxides/nitrides and conducting polymers, essentially store electric energy on their active surfaces through quick, reversible electrochemical redox processes.

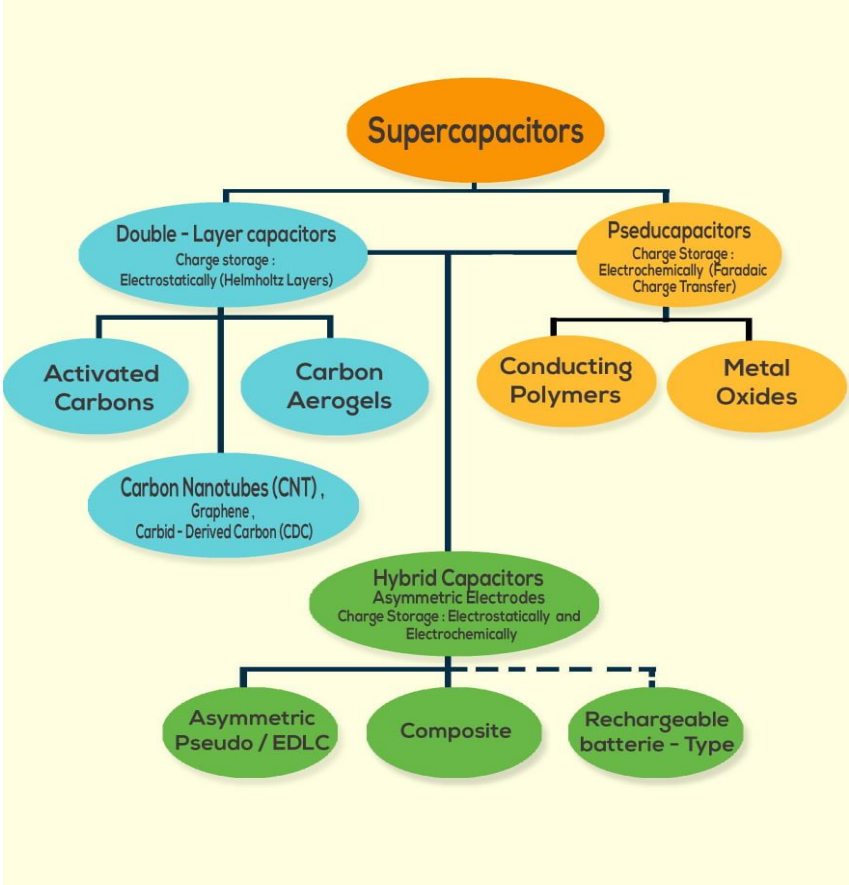

Figure. 1.3 Material and device classification for supercapacitors.

The following properties must be met by both mechanisms:

1. Porous with high surface area
2. Good electrical conductivity
3. Good wettability
4. Long cyclic stability (>100 cycles)
5. Thermodynamically stable over wide potential range

1.3.1 Electrochemical Double-Layer Supercapacitor

The Electrochemical Double-Layer Supercapacitor (EDLC) is a type of electrochemical double-layer supercapacitor. In this kind of EDLC, electrostatic adsorption of ions at the electrode interface occurs in the region of the electrolyte in order to store electric energy without the use of chemical reactions. Carbon-based materials with a high surface-to-volume ratio are commonly

used for this type of storage. The double layer charging and discharging technique is always used to store data in EDLC capacitors. However, surface redox reactions are possible, implying that charge storage in the EDLC may include changes in chemical bonding, demonstrating that it functions partially physically and partially chemically [10]. When compared to batteries, EDLC has a higher power density but a lower energy density. Grahame, Gouy, Stern, and Chapman advanced the EDLC theory after Hermann von Helmholtz.EDLC is made up of two electrical conductors coated with porous material, with a liquid or solid electrolyte filling the gap between the electrodes. Conduction occurs through it in both electrolytes. To avoid direct contact between electrodes in a liquid electrolyte, a separator made of non-conducting sheets with a large number of pores that allow ions to pass through it is placed between them, while in a solid electrolyte, the electrolyte itself serves as a separate that can transfer ions through it. The schematic of a typical two layer capacitor with charged and discharged states is shown in Figure. 1.4.

When the two electrodes are immersed in the electrolyte equal to two EDLCs connected in series, as shown in figure. 1.5, they become polarised. The capacitance at the surface of the cell's positive electrode (anode) is C_p, while the capacitance at the surface of the cell's negative electrode (cathode) is C_N. Figure 1.5 shows a schematic illustration of the EDLC potential distribution between the negative and positive electrodes in the electrolyte solution.

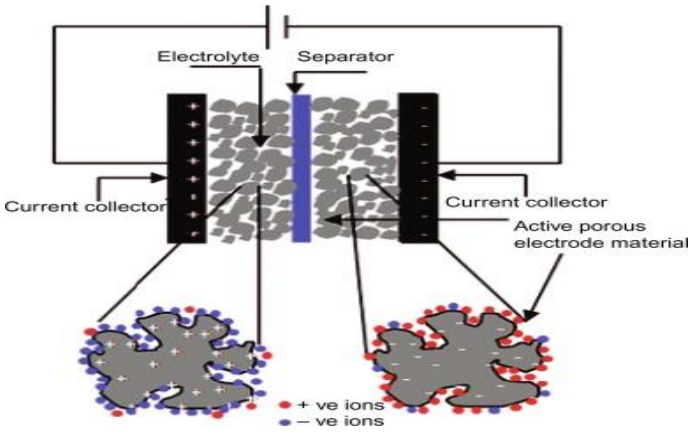

Figure. 1.4 Charged and discharged states of the negative electrode pore in the electrolyte are depicted schematically in an EDLC.

Helmholtz anticipated the occurrence of a double layer at the electrode surface for the first time in 1879, dubbed the Helmholtz layer. Chapman, Gouy, Grahame, and Stern later improved the

Helmholtz layer theory. The positive and negative charges in the electrolyte are organised in an array at the interface, with very tiny distances between them in order of atomic distance (~10Å). The quantity of charge accumulated by this assembly is determined by the electrode potential [11,12].

Carbon is commonly used as an electrode material in EDLC. It possesses good features for EDLC electrodes, such as abundance, large surface area, tunable shape, and high electrical conductivity. Carbon materials can be post-treated to change their structural and chemical/mechanical properties for a variety of purposes. In order to increase the capacitance (number of ions adsorbed) for EDLC applications, carbon structures must acquire a large surface area (in m^2/g). Pore size distribution can be reduced to attain these huge surface areas.

When the orifice of a pore is the same magnitude as the diameter of an ion (a solvated one in electrolyte solutions and a naked one in molten salts and ionic liquids), the surface area inside pores may become unreachable for solution and ions, resulting in a limit of useful porosity and possible surface area [13]. Another concern is that electrical conductivity is reduced as a result of the high surface area created by long and complicated electronic paths. Due to the large ESR values (electrical or equivalent series resistance) that result, it will limit charge and discharge rates, lowering the device's power density. Electronic characteristics can be controlled and improved by nitrogen doping or doping with other hetero-atoms [14]. As a result, the thickness of the films will grow, avoiding the practical implications. Natural sources exist for obtaining many appropriate morphologies, particularly porosities. Template technique [15] is an example of a synthetic procedure.

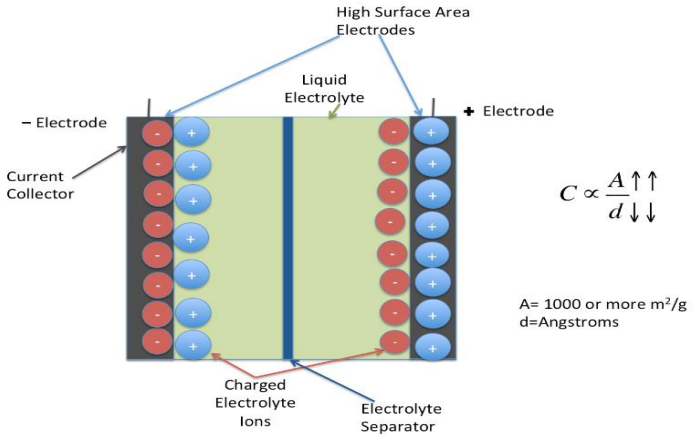

Figure. 1.5 Potential distribution in the electrolyte solution between the anode and cathode in an EDLC cell. (Source: from the Royal Society of Chemistry)

1.3.2 Pseudocapacitor

The mechanism at work in a pseudocapacitor differs from that of an EDLC. The charge is stored at the electrode/electrolyte interface due to columbic interaction in EDLC, which does not entail any chemical changes to the electrode surface. This type of storage is known as non-faradic storage. The mechanism in most pseudocapacitors is faradic in nature, and it is similar to EDLC. The carbon compounds effectively provide a surface area of roughly 2000 $m^2 g^{-1}$, implying a non-faradic charge storage mechanism. However, metal oxides effectively provide a surface area of 140 m^2 g^{-1}, which incorporates a faradic charge storage process. The main mechanism of pseudocapacitance is the oxidation and reduction reaction at the electrode surface [16]. The schematic representation of a pseudocapacitive SC electrode material displaying surface diffusion and intercalation faradic charge transfer is shown in Figure. 1.6.

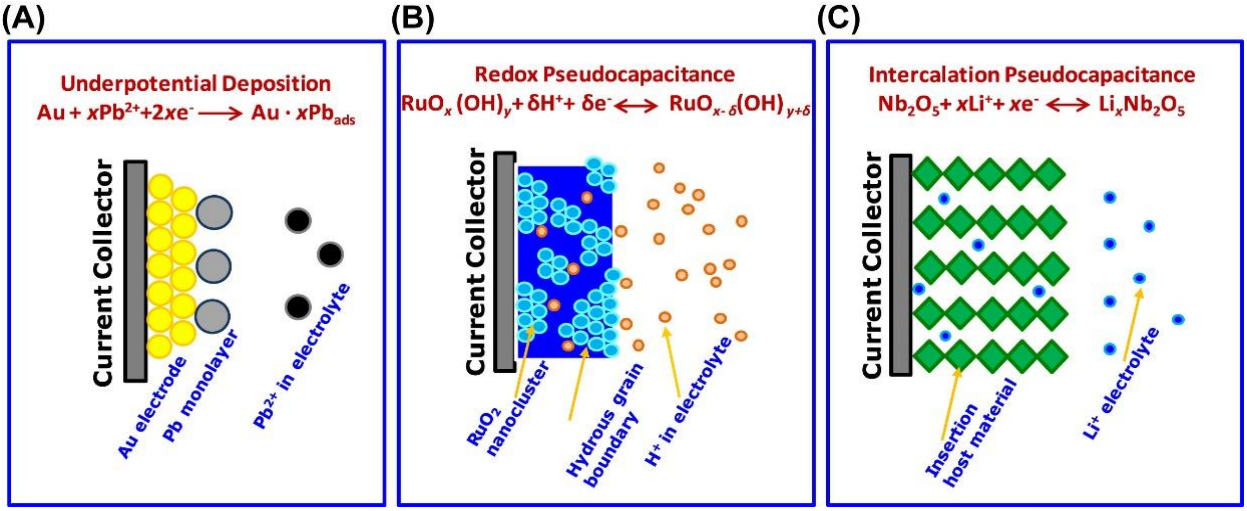

Figure. 1.6 Schematic diagram of redox pseudocapacitance and intercalation pseudocapacitance.

As demonstrated in figure. 1.6, the faradic charge transfer is responsible for pseudocapacitance, which occurs when ions pass the double layer at the electrode electrolyte interface via electrochemical adsorption. Intercalation of electrolyte ions into the layered structure of the active material, on the other hand, causes a faradaic charge-transfer reaction in the intercalation pseudocapacitance. Intercalation pseudocapacitance differs in that there is no crystallographic phase transition [17]. Metal oxides, which have three times the mass

loading of EDLC material in a given area, are commonly utilised as pseudocapacitor electrode materials. In fact, metal oxide-based SC takes up 40% less space than EDLC for the same capacity. Furthermore, the energy capacity of the pseudocapacitive SC can be up to 80% higher than that of an EDLC of the same size.

1.3.3 Hybrid Supercapacitor

Electrolyte is sandwiched between one current collector coated with double layer exhibiting material and another current collector coated with pseudocapacitance exhibiting material to create a hybrid SC. When compared to each other, the EDLC has a greater power density and the pseudocapacitive SC has a significantly higher energy density. The hybrid, which is a combination of these two electrodes, produces more power and energy density than symmetric SC made from individual electrode materials. The schematic diagram of a hybrid SC with activated carbon as the positive electrode and Li-doped graphite as the negative electrode is shown in Figure. 1.7. The charge storage mechanism in activated carbon is of the EDLC type, while Li doped carbon stores the charges by a pseudocapacitive intercalation process [18].

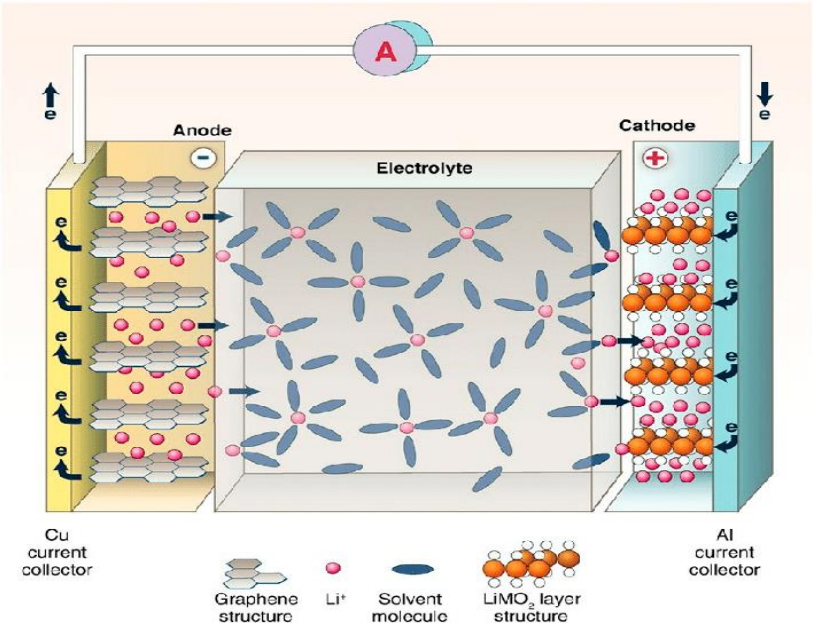

Fig. 1.7 Schematic diagram of hybrid SC representing Li-intercalation/de-intercalation into anode with EDLC at cathode.

1.4 Supercapacitor Components

The supercapacitor is made up of four parts [Figure. 1.8], each of which serves a specific purpose. The four components are:

(i) electrode
(ii) electrolyte
(iii) separator and
(iv) current collector

The capacitive, or Faradaic, mechanism stores charge in the electrode by interacting with electrolyte ions. Electrolytes offer the necessary ions for the charge/discharge process to take place. The separator works as a buffer, preventing system short circuits. To transport electrons, the current collector creates a conducting conduit from the electrode to the external circuit

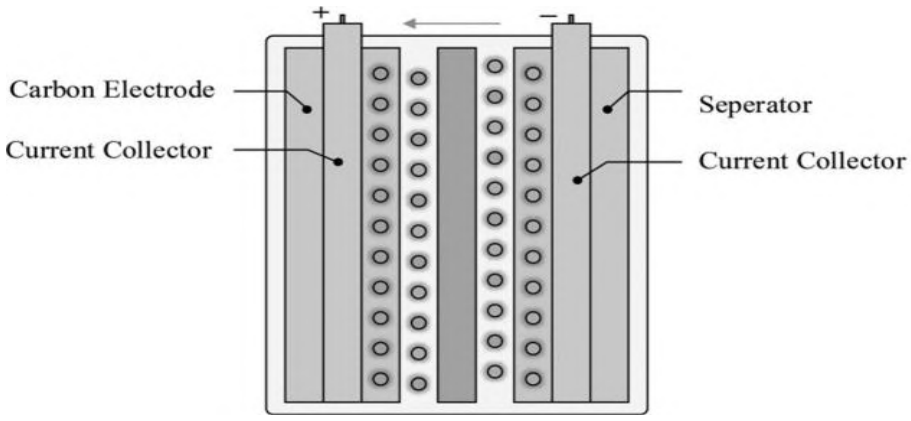

Figure 1.8 Construction of a supercapacitor.

1.4.1 Electrode.

Electrodes have a significant part in determining the output performance of a cell. Charges are stored when the potential is applied. It should be highly conductive to allow for quick electron transmission to the outside circuit. [19] The optimal electrode must meet the following requirements. membrane with a high specific area: Ions from the electrolysis react with the electrode's surface. More electrode material is revealed when electrolyte ions have a larger surface area. The basic capacitance and energy density of the electrode material are thus increased.

Mediated porosity: It has an impact on the capacitance and rate capabilities of the electrode material. The pore size must be larger than electrolytic ions to become adsorbed on the electrode surface.

High electronic conductivity:The material's rate capabilities were calculated, as well as its power density. Increased conductivity lowers resistance and allows electrons to go from the electrode to the current collector.

Electroactive surface sites:Pseudocapacitance is aided by electroactive surface spots that attract electrolytic ions. Pseudocapacitance occurs when many electroactive substances, such as oxygen and nitrogen, improve electrode material conductivity.

High thermal and chemical stability:During repeated charge/discharge cycles, ion motions are involved, which can raise the temperature of the system. Chemical and corrosion resistance are important for the electrode's material durability.

Low cost and environmentally friendly: The reduced electrode cost reduces the total cost of the supercapacitor system. Electrodes made of environmentally acceptable materials provide a long-term solution.

Depending on the charge-storing method in supercapacitors, the electrode material can be divided into two categories:

a) EDLC electrodes, which feed charges electrostatically to the electrode-electrolyte interface;

b) pseudocapacitive electrodes, which store charges via Faradaic processes.

1.4.2 Electrolyte

The electrolyte is a crucial component of an electrochemical energy storage system. Their physical and chemical properties are important in determining the cell's performance and quality. It has an impact on the capacitance, energy, and power density of the device, as well as its rate of ability, cycle life, and security. It balances the charges between the two electrodes. The choice of electrolytes is crucial because it has a substantial impact on the electrode-electrolyte interfaces. To date, no perfect electrolyte can meet all of the requirements for supercapacitor applications. For electrochemical devices, the basic criteria for electrolytes are as follows [19].

***Electrolyte conductivity*:** Electrolyte conductivity should be high in order to achieve a high-performance system. The conductivity of an electrolyte is determined by (a) ion mobility, (b) ion concentration, (c) the elementary charge, and (d) the quantity of valence of transportable ion charges.

Salt effect: Electrolyte conductivity varies depending on the solvent. In the same solvent, the conductivity of salt concentration varies a lot. The quantity of free ions determines an ion's conductivity. Therefore, ideal conductivity will improve the electrolyte's ionic conductivity.

Solvent effect: The solvent part has a significant impact on the conductivity of the electrolyte. The conductivity of an electrolyte is influenced by its viscosity and dielectric constants. Ionic mobility is affected by the dissociation of salt and viscosity, which is dependent on the dielectric form. As a result, a suitable supercapacitor solvent needs to be viscous and have a high dielectric constant.

Stability of electrochemistry: It has to do with the system's stability and protection. Electrochemical stability is determined by (a) the electrolyte's interaction with the electrode's substrate and (b) the electrolyte's constituent elements.

Thermal stability: in this type of system, the electrolytes are crucial for the system's high-temperature performance. Due to heat release, electrolytes should also be stable throughout repeated charge/discharge cycles. The thermal stability of an electrolyte is mostly determined by its composition, which includes salt, solvent, and additions. Aqueous electrolytes, organic electrolytes, and ionic electrolytes are the three types of electrolytes used in electrochemical devices.

Aqueous electrolytes, for example, provide high conductivity and capacitance at minimal cost. Although it has a limited voltage operating window, it results in a low energy density. This is due to a 1.23V potential difference in water electrolysis. Organic and ionic electrolytes can both be worked at higher potentials than usual, despite the poorer ionic conductivity of both electrolytes. The organic electrolyte is toxic and can be difficult to handle. Ionic electrolytes are more expensive and have a lower electrode surface access due to the greater ion scale.

1.4.3 Separator

A separator is required for the construction of a supercapacitor, which separates two electrodes to produce a barrier. A separator's primary function is to prevent the system from short-circuiting. It

allows for smooth ion flow within the supercapacitor while avoiding any chemical alterations. As a result, the option of dividers is a critical requirement for the unit's proper operation. The following are some of the basic separator attributes [19]:

- It needs to be non-conductive.
- It should have low ionic resistance because of the electrolyte ion permeability.
- It must be possible to moisten the electrolyte simply.
- It should provide mechanical support to the cell.

1.4.4 Current Collector

The objective of the current collector is to transmit electrons from the device to the external circuit. It should have a higher electrical conductivity to allow for the resistance-free flow of electrons from the electrode to the external circuit. Because different electrode and electrolyte materials are utilised in supercapacitor systems, the current collector should be corrosion resistant. It should also have a lot of mechanical strength because it supports the entire cell mechanically. Existing collector materials generally include aluminium, iron, and steel alloys. To reduce contact resistance, the active substance is painted over the current collector. To have powerful electrode surface areas, nickel mesh, metal foams, and carbon fabric have been employed [19]. This reduces contact resistance while also allowing for homogeneous electrode dispersion.Materials like glass, paper, and ceramics can be used as separators. Polymer-based separators are commonly utilised in supercapacitors due to their reduced cost, porous design, and adaptability.

1.5 Applications of Supercapacitors

The supercapacitor is a relatively new technology that has recently seen significant adoption. It has received a lot of interest in terms of its use in a variety of fields. The following are some of the uses for supercapacitors.

1.5.1 Memory Backup

As a short-term backup power source, supercapacitors have long been used in consumer electronics.Many appliances today include digital memory components, and even a momentary

interruption in the power supply would result in the loss of stored data. In such cases, a supercapacitor can operate as the power supply for a brief time, allowing data to be retained [20].

1.5.2 Electric Vehicles

Due to their energy efficiency and the ability to recover energy lost during braking, the use of SCs in electric vehicles has attracted a lot of interest in the technology, which appeals to energy conservation. Many of the current power sources being evaluated for use in electric vehicles are insufficient to meet vehicle acceleration needs. Fuel cells are promising because of their extraordinarily high energy density, but their power specifications are currently limited. A combination of fuel cell and supercapacitor technology can thus meet an electric vehicle's power and energy requirements [21].

1.5.3 Portable Power Supplies

SCs can be utilised as an energy storage device in systems that aim to improve power distribution reliability and quality. Static condensers (Statcons) and dynamic voltage restorers are two types of devices that try to adjust for voltage changes by injecting or absorbing power from a distribution line. As a result, such systems necessitate some type of direct current energy storage device from which energy can be extracted and stored. The energy density of the direct current storage device will determine the length of voltage disturbance that may be adequately compensated . The great majority of voltage fluctuations on the distribution bus are transient, lasting no longer than ten cycles. As a result, the supercapacitor's limited storage capacity is not an issue. Because the storage device must be able to respond quickly to voltage fluctuations, the SC has the benefit of having a short discharge time [22].

1.5.4 Electromechanical Actuators

For the launch of a rocket, electromechanical actuators can conduct thrust vector control. Submarines can use them as flood control actuators or as space spacecraft. The majority of actuations Pulsed currents with high peak power consumption are required by systems. Average power requirements are moderate. While a supercapacitor bank by itself is unlikely to be able to store enough energy, a battery in conjunction with a supercapacitor could. It's possible to construct

it to fulfil both typical and peak load demands. Attempting to satisfy both with just a battery, the requirements result in an enormous configuration, which isn't ideal.In space applications, where weight must be kept to a minimum, this is undesirable. When compared to using a battery alone, a hybrid power source consisting of a battery and a SC bank can save 60 percent in weight [23]..

1.5.5. Portable Power Supplies

Supercapacitors are ideal for use as rechargeable standby batteries. Static condensers (Statcons) and dynamic voltage restorers are two types of devices that try to adjust for voltage changes by injecting or absorbing power from a distribution line [24].

1.5.6 Portable Electronic Equipments

Supercapacitors are ideal for use as rechargeable standalone power sources in portable electronic equipment with low energy consumption. Most devices that use battery power supplies currently have extensive recharge times and must be charged overnight. This has become acknowledged as a present technical restriction, but supercapacitors provide the possibility of creating gadgets that can be recharged quickly, maybe in a matter of seconds. It is possible to charge and discharge repeatedly without suffering significant efficiency loss [25].

1.5.7 Remote Power Supply from Renewable Sources

Energy storage is required for remote power suppliers that receive their energy from intermittent sources such as wind or solar radiation to ensure that energy is available at all times. SCs have a variety of advantages over the typically used battery in such situations. Continuous cycling has a negative effect on batteries in photovoltaic power systems, necessitating battery replacement every 3-7 years [26]. On the other hand, SCs can sustain a huge number of charge-discharge cycles without losing performance, so they only need to be replaced every 20 years, which is the lifetime of solar panels [27]. As a result, lifecycle costs are decreased by eliminating the need for periodic maintenance. Supercapacitors can also be employed on their own to provide the energy required by power quality systems, which ensures that power distribution is stable and uninterrupted. SCs then provide the energy required to inject electricity into the distribution line, compensating for

any voltage variations. They can also be utilised to create systems that allow for variable speed drives and the capacity to ride through power supply interruptions. Such applications are important in the industrial setting because they can prevent material and financial losses caused by machine downtime [28,29].

1.6 Literature Survey of Transition Metal Oxide for Supercapacitor Application

SCs have the potential to store energy from non-conventional sources [30]. Several attempts to combine the power density of capacitors with the energy density of batteries have been made in SC [31]. As a result, for many years, scientists have been researching the synthesis of competent electrode materials for SC applications. Activated carbon, graphite, carbon cloth, carbon aerogels, and carbon with various nanostructures are the most common SC electrodes used in EDLC. Conducting polymers, metal oxides, and hydroxides, such as RuO_2, MnO_2, Co_3O_4, NiO, $Co(OH)_2$, $Ni(OH)_2$, and others, are the most often utilised pseudocapacitive materials [30,32-36].Metal oxides have been identified as a suitable material for SC applications due to qualities such as strong conductivity and a variety of oxidation states, which can potentially supply significant energy and power in SC. Metal oxides such as ruthenium oxide (RuO_2), nickel oxide (NiO), cobalt oxide (Co_3O_4), iridium oxide (IrO_2), and manganese oxide (MnO_2) have all been extensively investigated as electrodes for pseudocapacitors. When employed as SC electrodes, metal oxides exhibit pseudocapacitive behaviour, with extraordinarily high specific capacitance values. However, most of these metal oxides have drawbacks in terms of toxicity, cost, and availability. The majority of research is focused on the development of fabrication technologies and composite materials to substitute an alternative electrode material in order to minimise cost while maintaining performance.

Transition metal oxides (TMO) offer unique features, such as pseudocapacitive property due to variable valance, which permits electrons and ions to be intercalated into the lattice, making them a good choice for SC use. However, they have a low capacitance when it comes to practical applications. Mixed transition metal oxides have made significant progress (MTMO). When compared to single metal oxide, the synergetic effect can enhance working potential and

capacitance [37]. $NiCo_2O_4$, $ZnCo_2O_4$, $MnCo_2O_4$, $ZnFe_2O_4$, $CoMoO_4$, $MnMoO_4$, ZnV_2O_4, $NiMnO_3$, and other transition metal oxides have been described in the literature [38-45].

1.7 Literature survey of Lanthanum-Based Perovskite Oxides for Supercapacitor Application

Due to its high density and oxygen vacancy concentration, ABO_3 shows significant promise as an active material for SCs. Due to their superior thermal stability, easy synthesis, oxygen storage, low cost, and increased electrical conductivity, lanthanum-based perovskite oxides have sparked a lot of interest in SCs in recent years [46]. The first lanthanum-based perovskite oxide to be used in SCs is $LaMnO_3$. $LaMnO_3$ has a relatively stable and consistent oxygen excess because to the defective cation-deficient lattice and the presence of manganese in two oxidation states [47]. Mefford et al. reported a specific capacitance of around 609.8 F g^{-1} for $LaMnO_3$ in 2014 [48].

Silva *et* al. investigated La_2CoMnO_6 ceramic samples obtained by polymeric precursors method calcined at different temperatures. Structural analysis showed that fine-grained materials presenting single phase monoclinic structure were obtained for calcination temperature ranging from 700˚C to 1000˚C. XPS analysis showed that B-site cations are in the Co^{2+} and Mn^{2+} oxidation state. The site ordering can be improved by changing the calcination temperature and, simultaneously echoing in changes of the intrinsic dielectric and magnetic properties of La_2CoMnO [49].

Murthy *et* al. investigated the magnetodielectric (MD) behavior of La_2CoMnO_6 nanoparticles prepared by sol-gel method. Magnetic characterization revealed two distinct ferromagnetic transitions at 218 K and 135 K that can be assigned to ordered and disordered magnetic phases of La_2CoMnO_6 nanoparticles. A large MD response of 10 % and 8 % at 100 kHz were found at the dipolar relaxation peaks under 5T magnetic field. The dc electrical resistivity showed an insulating behavior and showed a negative magnetoresistance (MR). Impedence analysis supports both intrinsic and extrinsic effects for the observed MD response. At high temperature MD response majorly originated from the extrinsic effects such as MW capacitor model combined with MR [50].

Filho *et* al. synthesized Ln_2MnCoO_6 (Ln = La and Dy) by the combustion method and studied their structural and magnetic properties. XRD analysis reveals that the La_2MnCoO_6 (LCM) and Dy_2MnCoO_6 (DCM) samples have different coexisting crystal structures, the LCM consists of a mixture of crystalline orthorhombic, monoclinic, and rhombohedral phases whereas DCM consists of a mixed composition of hexagonal and orthorhombic structures. Magnetic measurements show that the magnetic transition temperature T_c decreases from 150K to 85K when the La ions are replaced by Dy and the magnetic order changes from a ferromagnetic to a ferromagnetic when La replaced by Dy [51].

Silva *et* al. studied the infrared relativity spectra of La_2CoMnO_6 (LCMO) ceramics obtained from a modified Pechini's method to determine the phonon contribution to that intrinsic dielectric response of the system and to investigate the Colossal Dielectric Constant (CDC) origin. The analysis shows that CDC effect of LCMO is of pure extrinsic origin, also estimated the dielectric constant and quality factor of the material in microwave region, which shows that LCMO is appropriate for application into microwave devices and circuitry [52].

Yousif *et* al. synthesized $LaCo_{.2}Mn_{0.8}O_3$ perovskites and La_2CoMnO_6 double perovskites by the modified sol-gel route with citric acid as combustion agent and got that these materials having orthorhombic structure. The as-prepared perovskite materials exhibit ferromagnetic nature. Electron Spin Resonance (ESR) measurements suggest the occurrence of Jahn-Teller glass analogous to the spin- glass behavior. The high value of dielectric constant for LCMO nanoparticle systems may be used in electric tunable devices [53].

Guo *et* al. reported that La_2MMnO_6 perovskites with M = Co, Ni, and Zn display the magnetic and dc conductive properties that obey the ordinary structure-property relationship, i.e., 3d electronic configuration, crystal/ electronic structure and physical property. The Cu sample shows a special Jahn-Teller configuration, giving rise to the degenerated e_g states and significant change in bond parameter. Consequently, the Goodenough- Kanamori rules are not followed and the ferromagnetic coupling is very low. The J-T effect causes a strong electron-phonon coupling which generates suitable hopping channel for small polarons, raising considerably its conductivity [54].

Yang *et* al synthesized La_2CoMnO_6 sample in an oxygen atmospheres, has a monoclinic structure at the room temperature. The lattice parameter of this sample from 120 K to 1400 K show the

monoclinic- rhombohedralral transition at ~ 450 K, and the ferromagnetic transition is at ~ 230 K with a small antiferromagnetic ordering at about 170 K. The strain analysis of lattice parameter data reveals the magnetoelastic coupling of La_2CoMnO_6 such that coupling of the magnetic moment is associated with volumetric and shear strains. This will facilitate its potential application in the field of spin electronics and thin-film engineering [55].

Fu *et* al. prepared La_2CoMnO_6 nanofibres through electrospinning. The results show that the prepared La_2CoMnO_6 nanofibers are stable, one dimensional structure with a diamond like crystal structure. The specific surface area of the fiber is 79.407 $m^2 g^{-1}$. The specific capacitance of the electrode material reaches 109.7 Fg^{-1} at a current density of 0.5 Ag^{-1}, indicating good electrochemical performance and good cyclic stability [56].

Meng *et* al. prepared hollow spherical porous La_2CoMnO_6 (HS- LCMO) by impregnating carbon sphere template. The hollow spherical porous material possesses large specific surface area. At current density of 1 Ag^{-1}, the specific capacitance of HS- LCMO (376 $Fg^{-1)}$ was 4-fold higher than that of reference sample (94 F g^{-1}). It has high energy density up to 65.8 Wh kg^{-1} at 1000 W kg^{-1}. The supercapacitors devices maintained around 89.2%of the initial capacitance after 3000 cycles. The material is suitable for high-performance energy storage for future [57].

Jashandeep *et* al. synthesis La_2CuCoO_6 double pervoskite by hydrothermal method and X- ray diffraction pattern confirmed the formation of monoclinic phase with $P12_1/cl$ symmetry. The transmission electron microscopy results confirmed the formation of self- assembled porous rods. The specific surface area of these mesoporous rods with an average pore diameter of ~ 6nm was ~ 41 m^2/g. The material specific capacitance of 259.4/g at current-d density of 0.5 A/g. It showed a long- term cyclic stability with ~89% specific capacitance retention at a constant current density of 4 $A.g^{-1}$ after 1000 charge/discharge cycles [58].

1.8 Objectives of the Present Work

Supercapacitors are an alternative to electrochemical batteries in energy storage applications because of their high power density and ultralong cycle life. However, in the current push to push the entire technology ahead to fulfil the benchmark requirements for commercialization, the comparatively low energy density is the main hurdle for supercapacitors. Because the electrode

used is intimately related to the specific capacitance and energy density of supercapacitors, developing electrode materials with outstanding electrochemical performance is critical to effectively solving this issue. Perovskite oxides have received a lot of interest as a possible electrode material for supercapacitors because of their unusual structure, compositional flexibility, and intrinsic oxygen vacancy.

The main objectives of this research work are as follows:

- To synthesize lanthanum-based double perovskite oxide nanomaterials especially La_2CoMnO_6 using facile low cost modified combustion method.
- To study the formation, stability, existence of crystalline phases, porous structures and surface properties of the prepared double perovskite oxide nanomaterials using different spectroscopic and microscopic analytical techniques.
- To measure the as-synthesized electrode materials for electrochemical characterizations and performance analysis
- To check the stability of the fabricated electrode materials by GCD measurement with repeated cycle.
- Testing and electrochemical performance evaluation of energy storage module (supercapacitor) in applications.

CHAPTER 2

SYNTHESIS AND CHARACTERIZATION TECHNIQUES

The synthesis of the compound chosen for this study, as well as the experimental methodologies used to characterize the specimen, are discussed in this chapter.

2.1 Introduction

Ceramic materials are particularly important in materials science because of their direct and indirect applications in everyday life. Hence, the synthesis of novel ceramic powders is critical. For the preparation of ceramic materials, a range of synthetic procedures have been used, including solid state reaction, co-precipitation, sol-gel, and ball milling. Each approach has its own set of pros and disadvantages when it comes to achieving a high-quality product in terms of purity, homogeneity, reactivity, particle size, and so on. In this context, the auto-ignition solution combustion approach, in particular, is found to be more convenient, and less expensive technique than other accessible methods in terms of performance, reliability, reproducibility, and economy.

2.2 Auto-Igniting Combustion Synthesis

The synthesis of nanoparticles of ceramic oxide powders using auto-igniting solution combustion is a straightforward approach that uses metal salts that are even insoluble in water. The compound could be a single component, a two-component system, or even a multi-component system. In this phase, pure ultra-fine powder is obtained using only a hot plate and a ventilated fume hood in this procedure, which avoids extended calcination at high temperatures. This technology is so unusual that it can produce single phase ceramic oxide with complicated systems in nano-particulate form. The following are the steps of the ultra-fine ceramic oxide powder synthesis procedure:

a) Make a solution of all the metal salts and mix them in the proper proportions.
b) Add the needed amount of citric acid to the solution as an organic complexing agent.
c) The addition of the required urea as a fuel.

d) Adding concentrated HNO_3 to the system to adjust the nitrate concentration

e) Heating the solution with a hot plate.

Figure 2.1 - Flowchart depicting combustion synthesis route of nanopowders.

Metal salts can be made from alkoxides, oxides, nitrates, oxychlorides, carbonates, or any other substance that can be dissolved in the same solvent. After that, the salt solutions were mixed together, and an equal amount of citric acid was added. The equivalent ratio is the ratio of the metal nitrates' total oxidising and reducing valencies to the sum of the fuel/ complexing agent's total oxidising and reducing valencies. The precursor was given the proper amount of urea, which acts as a fuel. The oxidizer, concentrated HNO_3, was added to the combined solution to produce a clear, transparent solution. The solution was cooked on a hot plate and is acidic in nature. The solution boils and dehydrates, then decomposes, resulting in a smooth deflation with massive swelling, which produces foam. The foam then ignites, resulting in a voluminous and fluffy combustion product. Jose et al. [59, 60] employed citric acid as the complexing agent instead of polyvinyl alcohol, and urea or glycine was replaced with ammonia for the manufacture of nanoparticles of certain ceramic oxides utilizing the modified combustion process. To achieve reaction repeatability, synthesis parameters such as temperature, pH, reactant concentration, and time should be

properly associated with factors such as super saturation, nucleation and growth rates, surface energy, and diffusion coefficients. The synthesis pathway of several niobate systems of nanopartic1es is depicted in Figure 2.1. Figure 2.2 depicts the whole auto-ignition combustion processing phase. The auto-ignition solution combustion synthesis method was used in the current method for the manufacture of the title compounds. A number of trials were conducted to optimize the precursor solution for the synthesis of these chemicals.

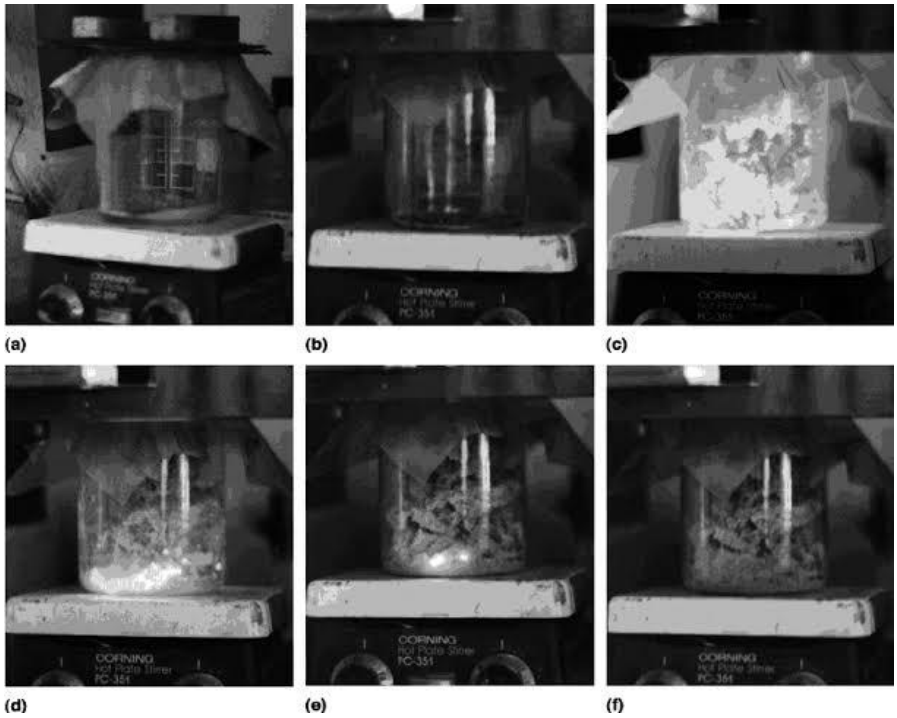

Figure 2.2 Photographs of different stages of combustion process for nanocrystalline powders. (a) Clear starting precursor, (b) Turned into gel, (c) and (d) Combustion processes, (e) combustion about to complete, (f) fluffy product from combustion.

2.3 Characterization Techniques

The present investigation employs experimental methodologies to investigate and characterize materials generated by a wet chemical combustion route (auto-ignition solution combustion technique). The materials were characterized in the following manner in this study: X-ray diffraction (XRD), Raman spectroscopy (FT-Raman), and Fourier transform infrared spectroscopy (FTIR) are used to investigate the structures of substances. Transmission electron microscopy

(TEM) is used to examine the particle size and shape. Scanning electron microscopy (SEM) was used to investigate UV-visible (UV-Vis) absorption, microstructure, and surface morphology.

2.3.1 X-Ray Diffraction (XRD)

X-ray diffraction (XRD) is an important non-destructive technique used to study the crystal structures and atomic spacing by analysing all kinds of matter ranging from fluids to powders and crystals. In 1912, a German physicist von Laue reasoned that if crystals were composed of regularly spaced atoms which might act as scattering centres for X-rays, and if X-rays were electromagnetic waves of wavelength equal to the interatomic distance in crystals, then it should be possible to diffract X-rays using crystals [61].

Bragg provided an alternative explanation for the measurement of diffraction of monochromatic X-ray from single crystals after Laue discovered of X-ray diffraction. He assumed that crystals are in layers or atomic planes (lattice planes-hkl) with spacing, d. When X-ray beams fall on the atoms or molecules of a crystal lattice, they get scattered. At certain incident angles of the X-ray beams, the scattered X-rays interfere constructively and a diffraction pattern is produced.

According to Bragg's law, the scattered X-rays will interfere constructively only if the path difference between the beams is an integral multiple of the wavelength of the X- rays. Bragg's law is expressed as,

$$n\lambda = 2d\ sin\theta$$

where, n is the order of diffraction, λ is the wavelength of the incident X-rays, d is the interplanar spacing and θ is the diffraction angle.

The X-ray diffractometer consists of three basic elements: An X-ray tube, a sample holder and an X-ray detector. X-rays are generated in a cathode ray tube by heating a filament to produce electrons which are accelerated towards the target by applying a voltage and bombarding the target material with the electrons. Characteristic X-rays are emitted when electrons have enough energy to dislodge the inner shell electrons. This X-ray signal is recorded and processed by a detector,

which then converts it to a count rate, which is then sent to a system like a printer or a computer monitor as output.

The average crystallite size was calculated using the Scherrer formula given by,

$$D = \frac{k\lambda}{\beta cos\,\theta}$$

where D is the average crystalline size, κ dimensionless shape factor, β line broadening at half the maximum intensity (FWHM).

The XRD machine is used in this research work have the following specification: Bruker D8 Advance Model with $Cu\ K\alpha$ radiation having wavelength $\lambda =$ 1.5409 Å, diffraction angle 2θ from 10º to 90º.

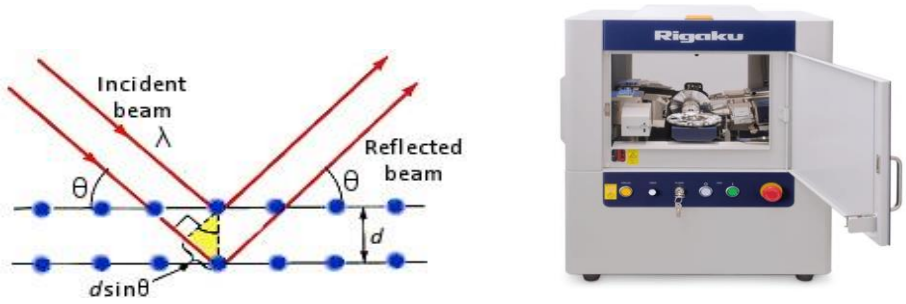

(a) **(b)**

Figure. 2.3 (a) Schematics of X-ray diffraction pattern (b) X-ray diffractometer.

2.3.2 Field Emission Scanning Electron Microscope (FE- SEM)

FE- SEM can be used to characterize the surface structure in great detail. Surface topography may be investigated with ease using a high-resolution FE- SEM down to the nm scale. The operating magnification can be changed between 0% and 100%. Magnification ranges from 10 X to 300,000 X, with a greater depth of field of more than 100 times magnification than optical microscopy [62]. Due to the limitations imposed by the optical wavelength, which is the primary bearer of surface information, optical microscopy is limited in its applications. However, by using fast moving electrons with high energy, reduced the wavelength that is shorter than the wavelength of light. In the SEM, thermionic emission is used to produce the majority of the electrons. Electric field

emission, on the other hand, can be used to generate a beam. FE-SEM refers to a scanning electron microscope with a field emission electron beam generator.

Figure 2.4 depicts the FE-SEM schematics. It is made up of three high-vacuum sections. For the creation of electron beams, the top is usually equipped with a field emission system. The magnetic apertures with objective lenses in the middle compartment concentrate the outgoing electron beam towards the target surface. On the bottom, there are places for sample holders and various detectors. The typical image of the sample surface is created by counting the number of electrons emitted at a certain surface where the SEM beam is focused, which results in pixel colour and hence the surface topography [63].

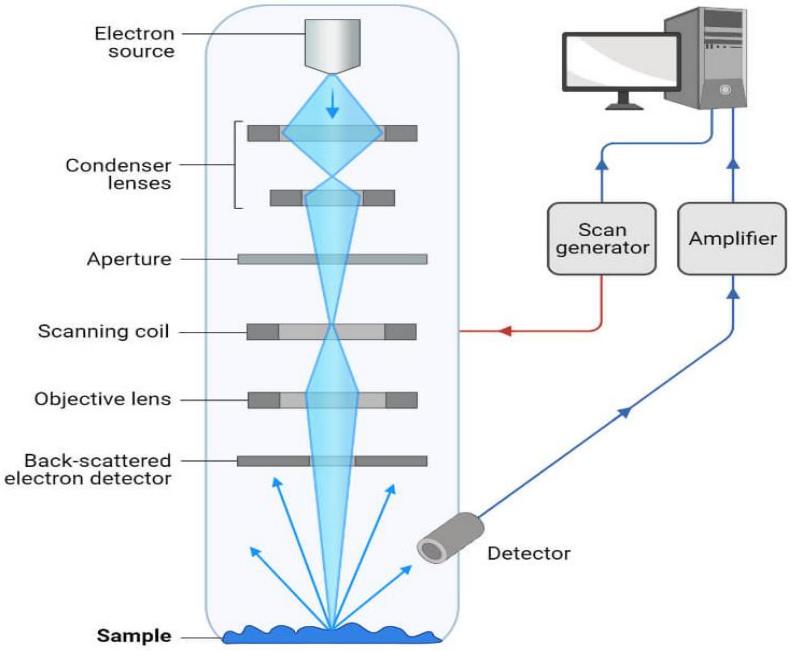

Figure. 2.4 Schematic for the operation of FE-SEM.

When a fast moving electron beam impacts the surface of a specimen sample, several interactions occur, resulting in distinct signals such as SE, BSE, and X-rays from the sample surface [63], all of which are features of the sample's lattice structure. The incident beam electron interacts with the lattice in a variety of ways, including inelastic scattering from the electron cloud surrounding the atom and elastic scattering from the nucleus. If the transferred energy is less than the work function of the material, electrons will not leave the surface in inelastic scattering. If the

transmitted energy is greater than the work function, however, the electron can leave the surface. Secondary electrons (SE) are expelled electrons with an energy of less than 50 eV that are formed at a distance of a few nm from the surface. Primary electrons are emitted electrons with a significantly higher energy than the work function. They cannot lose their energy due to elastic scattering by the atomic nucleus. Backscattered electrons (BSEs), which include Auger electrons, are released electrons with an energy greater than 50 eV. The energy of the primary beam electrons is roughly identical to that of the BSE. The principal electron energy ranges from a few hundred eV to 30 keV in the FE-SEM [63]. Secondary electrons, backscattered electrons, and elemental x-ray maps can all be used to create images in a FE-SEM.

2.3.3 Energy Dispersive Analysis by X-rays (EDAX)

When a rapidly travelling electron recoils the innermost electrons in inelastic scattering, causing electron holes in the innermost orbits, X-rays are emitted from the atom. As seen in figure. 2.5, the electron transition occurs to fill the innermost electron hole, resulting in the distinctive X-ray. Analyzing emitted distinctive X- rays from the sample surface can be used to do qualitative element identification [64]. Energy Dispersive X-ray Analysis (EDAX), or EDS, is a common technique for examining samples using the X-ray spectrum. Figure 2.5 depicts electron transfer events in an atom as a result of external stimulation.

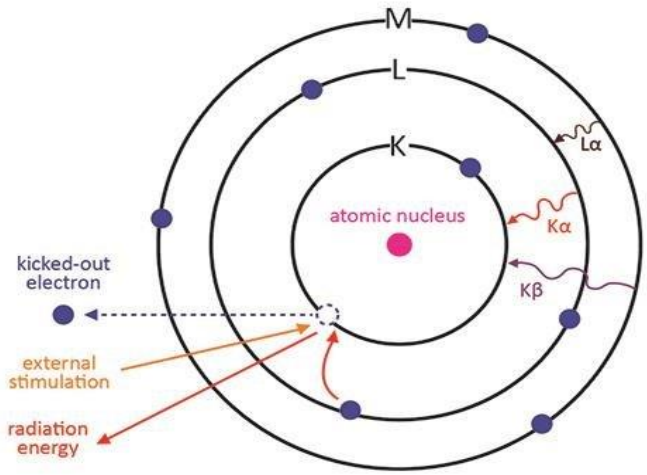

Figure. 2.5 Electron transfer process occurring in an atom due to external stimulation.

2.3.4 X-ray Photoelectron Spectroscopy (XPS)

When a sample is bombarded with monochromatic soft X-rays, the basic principle of XPS is that electrons are emitted from the sample surface. The kinetic energy of a released electron provides information on the binding energies of atomic orbitals, allowing surface chemical species to be identified. XPS (figure. 2.6) can be used to determine the relative concentration of species. The following [65, 66] `relationship can be used to calculate photon interactions with the core level.

$$KE = h\nu - BE - c\varphi$$

Where, $h\nu$ is the energy of an incident X-ray, and BE stands for the atomic orbital binding energy, $c\varphi$ stands for the spectrometer work function, and KE stands for the kinetic energy of the released electron. Each electron in an atomic orbital has its own unique binding energy. The electron kicked off from the innermost orbitals with their kinetic energy associated with the binding energy of the atomic orbital due to the absorption of incoming X-rays. Information about the state of elements can then be obtained by analyzing these energies. Peak intensity can provide quantitative information about an ingredient.

The following are the most commonly used monochromatic X-ray sources.

• $h\nu$ = 1253.6 eV for $Mg\ K\alpha$ radiation

• $Al\ K\alpha$ radiation has a wavelength of $h\nu$ = 1486.6 eV.

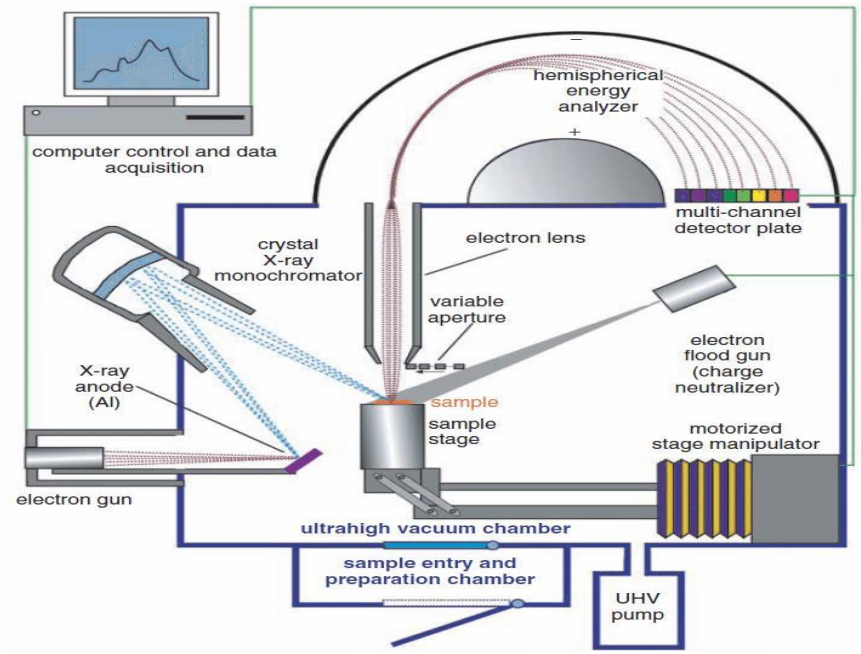

Figure. 2.6 Schematic of XPS.

The ejected electron can have an energy range of 0–1480 eV is excited by $Al\ K\alpha$ and $Mg\ K\alpha$ excites 0–1250 eV. Generally, due to the short inelastic mean free path of electrons this technique is very strong, it is very surface sensitive. The spectra were obtained on Thermo Scientific ESCALAB 250 Xi, using monochromatic Al Kα radiation (1486.6 eV). The obtained spectra were then analyzed.

2.3.5 Brunauer–Emmett–Teller (BET)

Brunauer–Emmett–Teller is a trio composed of Braeuer [67, 68], Emmett, and Tell (BET). BET is a technique for analyzing a specific surface area where gas molecules are physically adsorbed on a solid surface and is used for surface area analysis. The amount of gas adsorbed on the surface is determined by the available surface area, as well as the temperature, gas pressure, and strength of the gas-solid surface interaction. Because of its great purity and intense interaction with the surface, nitrogen gas is commonly used for analysis. The data from BET is shown as an isotherm, with the amount of gas adsorbed versus relative pressure depicted. There are five different forms of isotherms that can exist [67]. The specific capacitance of a supercapacitor can be determined by measuring the surface area and pore size of the produced material. The BET and BJH methodologies are necessary for this investigation to evaluate the effect of surface area and porosity change on electrochemical performance. The specific surface area was determined using Brunauer-Emmett-Teller (BET) method (BELCAT-M). Liquid nitrogen was used as adsorbent.

2.3.6 Raman Spectroscopy

This is an effective technique for analysing the vibrational and rotational modes of a sample material [68]. C. V. Raman is the name given to this type of spectroscopy. The primary mechanism entails the interaction of monochromatic laser light with phonons to produce various excitations in the systems, resulting in the inelastic scattering of monochromatic light in the visible, near infrared, or near ultraviolet ranges. Raman scattering is the name given to this type of scattering. The interaction involves the incident laser's energy changing, which provides useful information on the system's various vibrational modes.

The molecule relaxes into one of two rotational or vibrational states after excitation, which may or may not be the same as before excitation. Emitted photons carry away the energy difference

between the new and original states. The Stokes shift happens in the lower frequency zone when molecules relax to a higher energy level than their starting state, and the Anti-Stokes shift occurs in the opposite frequency region, as shown in figure. 2.7.

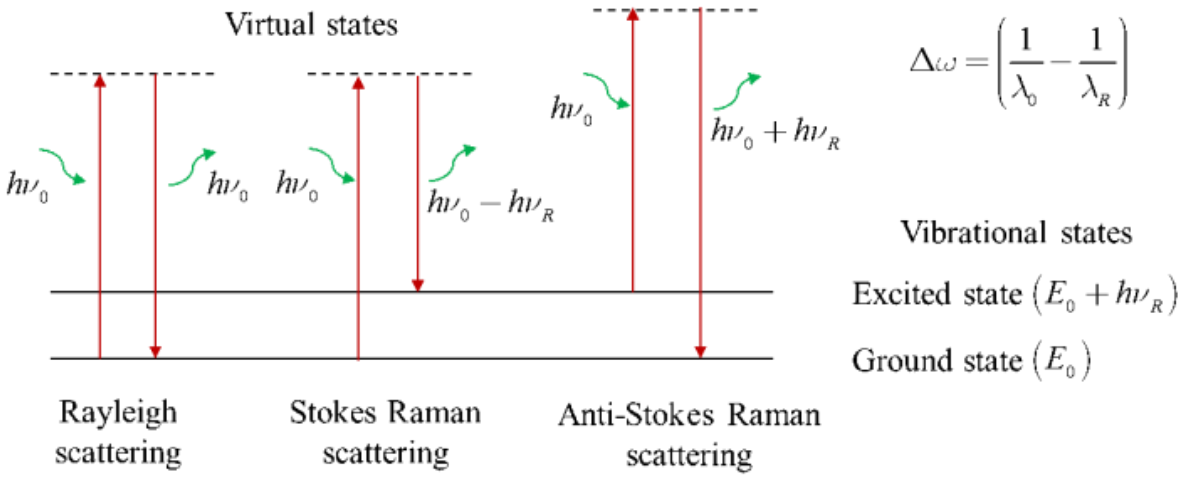

Figure. 2.7: Energy level diagram illustrating transitions involved in Rayleigh (elastic) and Raman (inelastic) scattering.

A Raman spectrometer consists of an excitation source, usually a laser, optics for sample illumination, a double or triple monochromator and a signal processing system consisting of a detector, an amplifier and an output device.

Figure. 2.8 Raman Spectrometer.

Renishaw micro-Raman spectrometer with a 2 mW charge coupled unit was used to record Raman spectra. The laser power was 30 mW, and the spectral resolution was 1 cm^{-1}.

2.3.7 Fourier Transform Infrared Spectroscopy (FTIR)

Infrared spectroscopy is used for to study what molecules present in the material. It also gives the type of bonds and vibrations occurred in sample, bond lengths between the atoms and so on. Commonly we measure the % transmittance of the sample in IR region with respect to the wave number. The Full range of the spectrum lies between 4000- 400 cm^{-1}. The expression for measuring transmittance is similar to the absorption spectroscopy.

$$\%T=100*\frac{I}{I_0}$$

where, %T= transmittance of sample in IR region

I= Intensity of IR spectrum of sample

I_0= Intensity background spectrum.

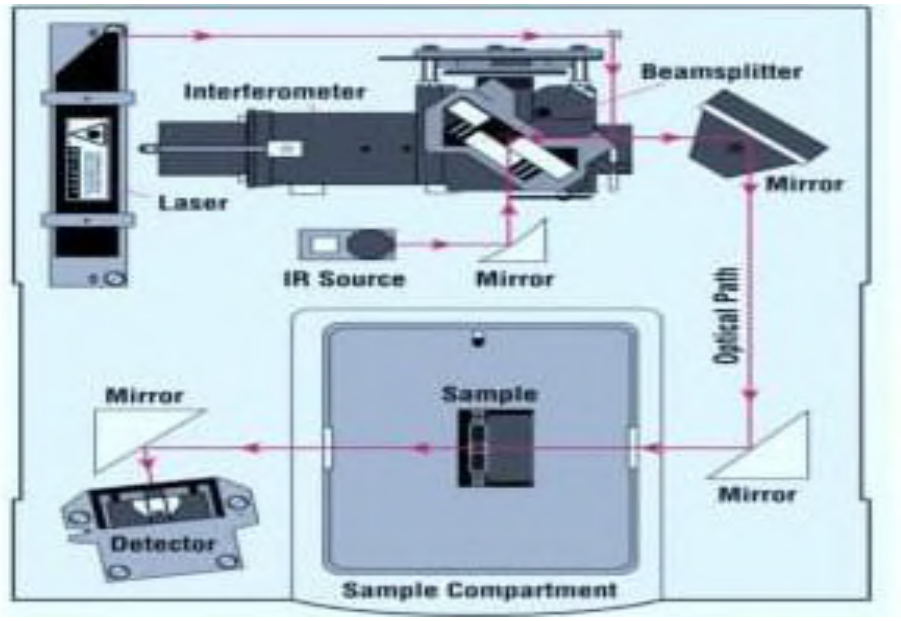

Figure. 2.9 Setup of FTIR spectrometer.

The main part of the spectrometer is interferometer. It measure the interference pattern of light from the source. Commonly Michelson interferometer is used in FTIR spectroscopy. In FTIR, IR

radiation is incident on the sample, in that time the molecules in the sample absorb IR radiation and goes to higher vibrational levels and remaining IR radiation passes through the sample and it received by detectors.

The main advantage of FTIR spectroscopy is it have low signal noise ratio due to this we get good transmittance spectrum. Increasing number of scans help to decrease the noises in the FTIR spectrum. It give rich amount of information about molecules, vibrations and structural parameters. The only disadvantages of FTIR spectroscopy is sometimes artefact developed in IR spectrum [69, 70]

2.3.8 Ultraviolet Visible Spectroscopy

Ultraviolet-visible spectroscopy is used to obtain the absorbance spectra of a compound in a solution or as a solid. Ultraviolet spectroscopy is also known as absorption spectroscopy or reflection spectroscopy as part of the ultraviolet and the fuel, adjacent visible spectral regions. This reveals that it uses light in the visible and also adjacent ranges. Atoms and molecules undergo electronic transitions. In this region of the electromagnetic spectrum, absorption spectroscopy is somewhat reciprocal to fluorescence spectroscopy, which deals with transitions from the excited state to the state, and in the absorption, it measures transitions from the ground state to the excited state [71].

The instrument which is used in ultra-violet spectroscopy is known as UV/Vis spectrophotometer. It measures the intensity of light passing through a sample (I) and compares it to the intensity of light before it passes through the sample (I_0). The ratio I/I_0 is the transmittance, and is commonly expressed as a percentage (%T). The absorbance, A< is based on the transmittance.

$$A = \log \left(\frac{100}{\%T}\right)$$

The fundamental parts of a spectrophotometer are a light source, a holder for the sample, a diffraction grating in a monochromator or a prism to separate the different wavelengths of light, and a detector. The radiation source used is a Tungsten filament (300-2500 nm), a deuterium arc lamp, which is continuous over the ultraviolet region(190-400nm), Xenon arc lamp, which is

continuous from 160 to 2000 nm; or a light emitting diodes (LED) for the visible wavelengths [72]. The detector is customarily a photomultiplier tube, a photodiode, a photodiode array or a charge coupled device (CCD). Single photodiode detectors and photomultiplier tubes are most commonly used with scanning monochromators, which will filter the light so that only light of a single wavelength reaches the detector at a time. The scanning monochromators, which will filter the light so that only light of a single wavelength reaches the detector at a time. The scanning monochromator moves the diffraction grating to step-through each wavelength hence its intensity may be measured as a function of wavelength. Fixed monochromators are used with CCDs and photodiode arrays. There are both single beam and double beam spectrophotometers. In a single beam instrument, all of the light passes through the sample cell. I_0 is measured by removing the sample. This is one of the earliest designs and is still in common use.

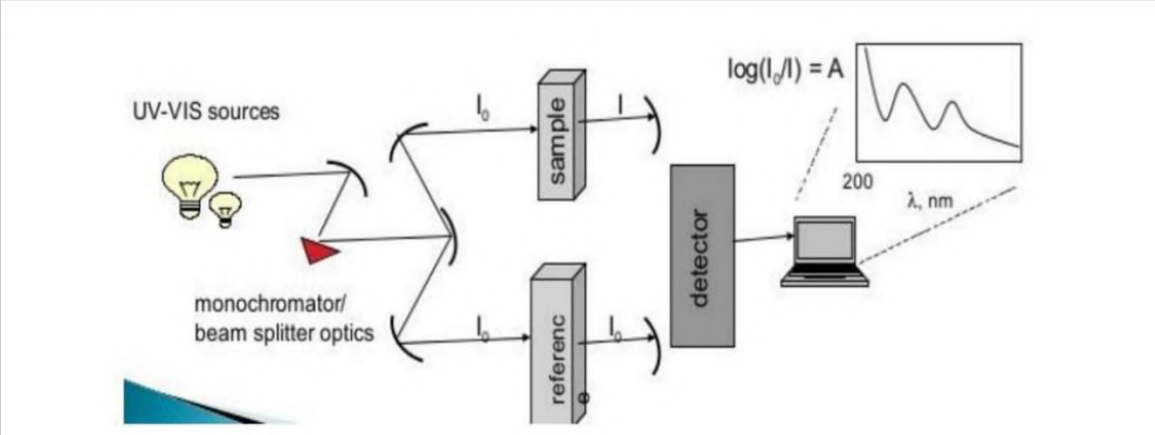

Figure. 2.10 Simple schematic diagram of spectrophotometer [73].

In a double-beam experiment, the light will split into two beams before it reaches the sample which is depicted in the above figure. Out of which one beam is used as the reference and the other beam passes through the sample. The reference beam intensity is taken as 100%. Transmission or Absorbance, and the measurement will be the ratio of the two beam intensities. Some of the double-beam instruments have two detectors, and the sample and the reference beam measured at the same time. The detector alternates between measuring the sample beam and the reference beam in synchronism with the chopper. There may also be one or more dark intervals in the chopper cycle. In this case, the measured beam intensities may be corrected by subtracting the intensity measured in the dark interval before the ratio is taken.

In a single-beam instrument. The cuvette containing only a solvent has to be measured first. Mettler Toledo developed a single-beam array spectrophotometer that allows fast and accurate measurements over the UV/VIS range. The light source consists of a Xenon flash lamp for the Ultraviolet (UV) as well as for the visible (VIS) and near-infrared wavelengths covering a spectral range from190 up to 1100 nm. The lamp flashes are focused on a glass fibre which drives the beam of light on to a cuvette containing the sample solution. The beam passes through the sample and specific wavelengths are absorbed by the sample components. The remaining light is collected after the cuvette by a glass fibre and driven into a spectrograph. The spectrograph consists of a diffraction grating that separates the light into different wavelengths, and a CCD sensor record the data, respectively. The whole spectrum is thus simultaneously measured, allowing for fast recording [72].

Sample for UV/Vis Spectrophotometry are most often liquids, although the absorbance of gases and even of solids cam also be measured. Samples are typically placed in a transparent cell, known as a cuvette. Cuvettes are typically rectangular in shape, commonly with an internal width of 1 cm. Test tubes can also be used as cuvettes in some instruments. The type of sample container must allow radiation to pass over the spectral region of interest. The most widely applicable cuvettes are made of high-quality fused silica or quartz glass because these are transparent throughout the UV, visible and near infrared regions. Glass and plastic cuvettes are also common, although glass and most plastic absorb in the UV, which limits their usefulness to visible wavelengths [74].

2.4 Electrochemical Measurement for Supercapacitive Behaviour of Electrode Materials

2.4.1. Fabrication of Supercapacitor Electrode

The electrochemical performance of the electrodes is analyzed with the help of a standard three - electrode system containing a Pt wire as a counter electrode and an Ag/AgCl (sat. KCl) as a reference electrode. The working electrode is manufactured by making slurry with active material (La_2CoMnO_6), acetyl black, and polytetrafluoroethylene (PTFE) according to a mass ratio of 85: 10: 5 in N – methyl – 2 - pyrrolidone (NMP). The mixture is coated evenly over the stainless-steel substrate. All the electrochemical measurements are carried out in a 1M Na_2SO_4 electrolyte medium.

2.4.2 Cyclic Voltametric Technique (CV)

Cyclic voltammetry (CV) is an effective electrochemical technique for determining the specific capacitance (Csp) of electrode materials used in supercapacitors. CV is commonly used to investigate the electrochemical evaluation of active material in an electrolyte solution for a specific application supercapacitor. It is a potentiodynamic process in which the potential of a substance is increased. At a constant voltage scan rate, the working electrode sweeps between two voltage limits [75]. It generates basic information about redox behaviour, specific capacitance, charge transfer kinetics, reversibility, and material stability, among other things, as shown in Figure 2.11.

To begin with, choosing an initial and end potential is a critical aspect of CV measurement. To reduce ohmic resistance, a three-electrode arrangement is used. A potential is provided between a reference electrode and a working electrode, and current is measured between the working electrode and a counter electrode. The range of operating potentials for a CV in various electrolytes varies and is dependent not only on electrode material but also on electrolyte composition. Furthermore, the redox potential of the material and the decomposition capacity of the electrolytes influence the operating potential window of the working electrode. In general, a positive potential limit is created by high current resulting from electrolyte oxidation, while a negative potential limit is caused by electrolyte reduction.

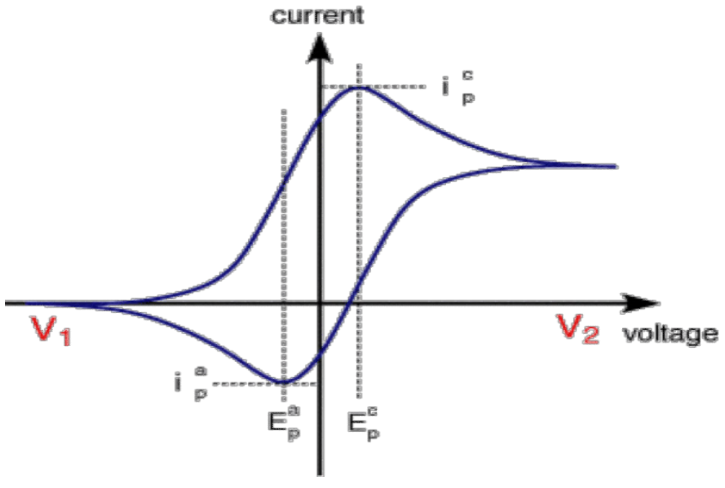

Figure 2.11. Cyclic Voltammogram.

The potential is swept in CV between two fixed values (i.e. inside a potential window). The scan swept back and the voltage reverted to point V_1 when the voltage reached pointV_2. The potential limits are V_1 and V_2, the cathodic and anodic peak currents are i_{pc} and i_{pa}, and the cathodic and anodic peak voltages of the resultant voltammogram are E_{pc} and E_{pa} During the forward scan, the current increases as the potential approaches the electroactive material's oxidation potential, but it decreases as the potential rises higher due to the high concentration of electrolytic ions at the electroactive sites. In a reversible redox pair, the product formed during the initial oxidation reaction decreases and creates reverse polarity current when the reverse potential is supplied.

As shown in fig. 2.8, the average capacitance is measured (C) in a typical cyclic voltammogram, as shown in the following relation.

$$C = \frac{I}{dv/dt} \tag{1}$$

Where, I is the current averaged over the cycle measured in amperes and $\frac{dv}{dt} = v$ is the scan rate in volt/sec.

The capacitance in a voltammogram is given by

$$C = \frac{1}{v(V_1 - V_2)} \int_{V_1}^{V_2} I(V) dV \tag{2}$$

Where, $(V_1 - V_2)$ = potential difference and $I(V)$is response current.

Interfacial capacitance (C_i) is expressed by the following equation.

$$C_i = \frac{C}{A} \tag{3}$$

where 'A' is the area (1 cm^2 in this study) of electrode in contact of the electrolyte.

The specific capacitance C_s (F/g) can be obtained by,

$$C_s = \frac{C}{W} \tag{4}$$

Where, W be the mass loading of active material under study.

2.4.3 Galvanostatic Charge-Discharge (GCD)

The measurement technique of galvanostatic charge-discharge (GCD), also known as chronopotentiometry (CP), can provide useful information on capacitance, energy density, power density, equivalent series resistance, and cycle life. A continuous current is applied to the working electrode in the GCD technique, and the accompanying potential with respect to a reference electrode is measured. The amount of charge transmitted between the electrodes remains constant when the working electrode charges and discharges at a fixed current density. The amount of change in potential and time is measured, and it varies depending on the current density used. Figure 2.12. depicts a charge-discharge curve schematic.

The two-electrode test cell, on the other hand, is ideal for determining the cycle life of supercapacitors because it is similar to more realistic operating conditions. The charge storage mechanism of a certain electrode is revealed by the nature of the charge-discharge curve. If the charge-discharge curve is linear, the charges are stored by an electric double-layer mechanism; otherwise, the charge-discharge curve is non-linear, implying that the charges are stored by a pseudocapacitive mechanism [76].

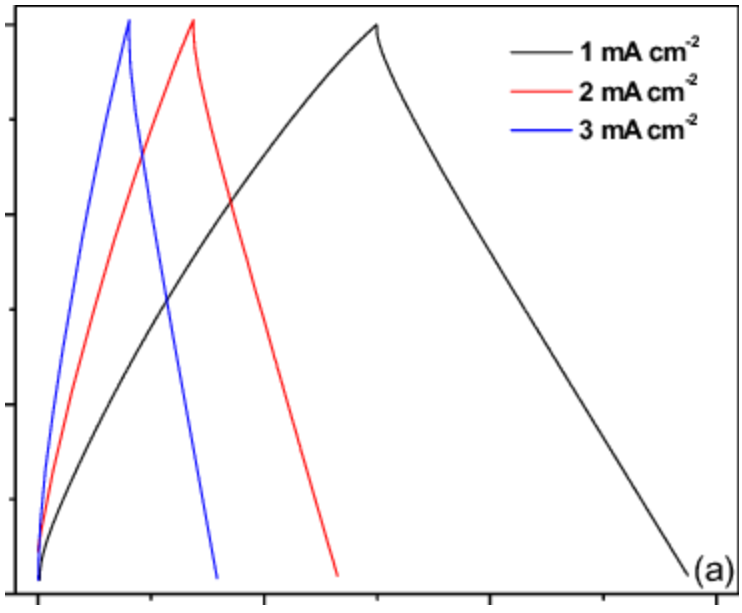

Figure 2.12. GCD Curve.

The capacitance measurement is used to investigate the redox reaction as well as the electrode materials' electrochemical properties. The electrode's capacitance can be estimated using the relationship.

$$C = Ix\frac{\Delta t_d}{\Delta V} \quad (5)$$

Where, I is the constant discharging current in ampere, Δt_d is the discharging time in second and ΔV $(V = V_1 - V_2)$ is the potential window.

2.4.4 Specific Energy Density and Power Density

GCD curves are used to reveal the electrode's specific energy and power density. Relationships 2 and 5 can be used to represent particular energy and power, respectively.

$$\text{Specific energy (SE)} = Qx\left(\frac{\Delta V}{W}\right) = \frac{I\ x\ t\ x\Delta V}{W} \quad (6)$$

$$\text{Specific power (SP)} = \frac{SE}{t} = \frac{I\ x\ \Delta V}{W} \quad (7)$$

Where, W is the mass of active material in Kg immersed in electrolyte.

2.4.5 Electrochemical Impedance Spectroscopy (EIS)

The electrochemical performance of the electrode and electrolyte system is investigated using the electrochemical impedance spectroscopy (EIS) technique. The frequency dependent impedance is measured (both resistance and reactance) [77]. The electrical impedance (Z) can be determined using the equation below.

$$Z = \frac{E(t)}{I(t)} = \frac{1}{Y} = \frac{E_0\sin(2\pi ft)}{I_0\sin(2\pi ft+\varphi)} \quad (8)$$

Where, voltage-time function $E(t)$ and the resulting change of the current-time function $I(t)$, E_0 and I_0 are the maximum voltage and current signals, f is the frequency, t is time, φ is the phase shift between the voltage-time and current-time functions, and Y is the complex conductance.

In simple setup, the frequency is varied from 1 Hz to 1 MHz under open circuit condition with given AC amplitude of 5 to 10 mV. The plot of Z_{re} Vs Z_{im} called Nyquist plot, a parametric graph of a frequency response and signal processing, was analysed to estimate the equivalent series resistance(R_S), the charge-transfer resistance (R_{CT}) at the interface between thin film and electrolyte [77].

CHAPTER 3

ELECTROCHEMICAL PERFORMANCE OF La_2CoMnO_6 DOUBLE PEROVSKITE

Double perovskite manganite materials like La_2CoMnO_6 are considered to be an outstanding candidate for the future generation memory gadgets due to their multifunctional properties like Curie temperature, magneto resistive effects, optical band gap etc. Recently, due to the high energy demand, La_2CoMnO_6 perovskite manganite was explored, as a suitable electrode material for high-performance supercapacitors. Hence, in this study, the structural, morphological, vibrational, optical properties and electrochemical performance of La_2CoMnO_6 manganite prepared using a modified combustion method are explored.

3.1 Synthesis of La_2CoMnO_6 double perovskite

La_2CoMnO_6 double perovskite manganite was prepared using a modified combustion method. Lanthanum (III) nitrate hexahydrate (99.9%), Cobalt (II) nitrate hexahydrate (99%), Manganese (II) nitrate tetrahydrate (98%) (all from Alfa Aesar, AR grade) were used as the precursors and citric acid anhydrous (Himedia) was used as the organic fuel. Stoichiometric amount of precursors and fuel were dissolved in distilled water on constant stirring without forming any precipitate. 30 ml of nitric acid is added to this mixture and its pH is maintained as neutral by the addition of ammonium solution. Then this complex solution is transferred to a hot plate, placed inside the combustion chamber, and heated at 250 ºC. On heating, the solution undergoes dehydration as well as internal combustion and thus a black coloured powder was obtained. This powder is then calcined at 600 ºC for 3 hrs and sintered at 700 ºC for 5 hrs in a high-temperature furnace to remove the water content and impurities. Then the resultant nanoparticles were taken out for various characterizations.

3.2 Characterization Technique

3.2.1 Structural analysis

The structure of La_2CoMnO_6 double perovskite over the 2θ range of 20° - 80° is examined using XRD and is given in Figure. 1. The main diffraction peaks identified at 2θ = 22.95°, 32.50°, 40.13°, 46.62°, 52.54°, 58.08°, 68.19°, 77.55° correspond to (110), (112), (202), (004), (222), (312), (224), (332) planes respectively and are in good agreement with the ICSD no. 98240 [78]**.** Since the sample is sintered at a low temperature (700 ℃), an additional peak corresponding to the secondary phase of manganese - cobalt spinel $MnCo_2O_4$ is present and is labelled with the asterisk symbol in Figure. 3.1.

Generally, the La_2CoMnO_6 double perovskites belong to orthorhombic and monoclinic structures. The orthorhombic structure corresponds to the random arrangement of cobalt and manganese along its octahedral perovskite sites, whereas, its monoclinic structure corresponds to the ordered arrangement of Co^{2+} and Mn^{4+} ions on its 2c and 2d sites [79]. Figure. 3.2 depicts the Rietveld refinement pattern of the La_2CoMnO_6, which confirms its monoclinic structure with a space group of $P2_1/n$. The structural and refinement parameters observed from the Rietveld analysis are tabulated in Table 3.1.

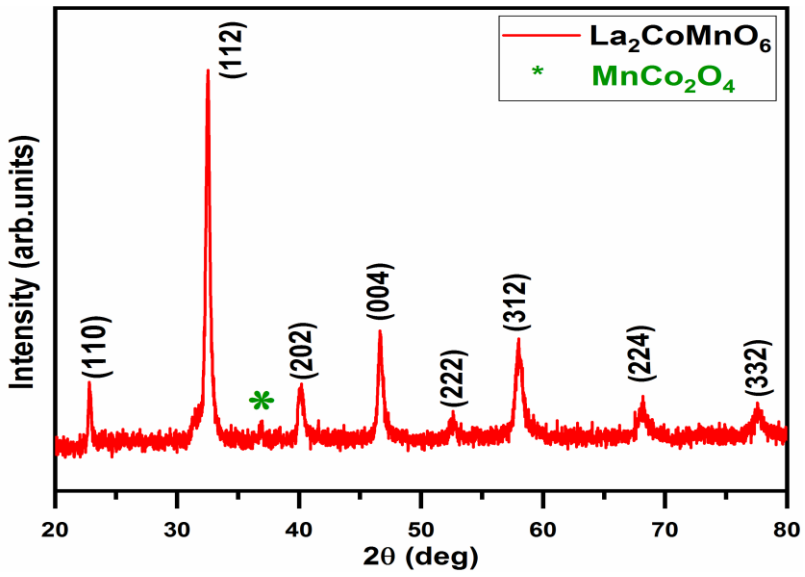

Figure. 3.1 XRD pattern of La_2CoMnO_6 double perovskites.

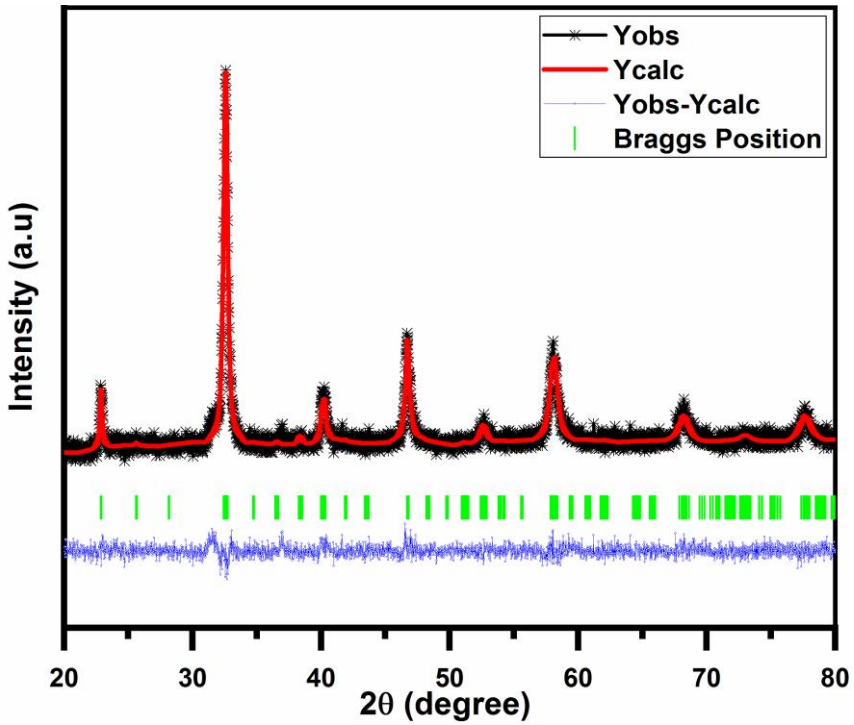

Figure. 3.2. Rietveld refinement pattern of La_2CoMnO_6 double perovskite.

The small deviation in β angle (89.8°) from 90° indicates the structural distortion present in the prepared sample, which can be determined using Goldschmidt's tolerance factor [80] equation,

$$t = \frac{r_{La} + r_O}{\sqrt{2}\left(\frac{\langle r_{Co}\rangle + \langle r_{Mn}\rangle}{2} + r_O\right)} \quad (1)$$

Where, $r_{La}\ and\ r_O$ denotes the ionic radii of La^{3+} and O^{2-} ions respectively. While $\langle r_{Co}\rangle\ and\ \langle r_{Mn}\rangle$ indicates the average ionic radii of Co and Mn ions. Generally, for double perovskites, tolerance factor ranges from t = 0.75 to 1. In our present study, it is found to be 0.90, which further confirms its monoclinic structure**.**

The average crystallite size (D) of La_2CoMnO_6 nanoparticles is determined by Debye – Scherrer formula,

$$D = \frac{k\lambda}{\beta cos\,\theta} \quad (2)$$

Where k stands for the dimensionless shape factor (0.89), λ is the wavelength of X- ray radiation (1.5406 Å), β is the full width at half maximum (FWHM) of the peak and θ represents the diffraction angle in degrees while its dislocation density can be determined using the equation,

$$\delta = \frac{1}{D^2} \quad (3)$$

The average crystallite size and dislocation density of La_2CoMnO_6 double perovskite is about 14.86 nm and 0.0045 nm^{-2}. The crystallite size and micro strain of the prepared sample can also be determined using the Williamson – Hall (W-H) method, using the relation,

$$\beta cos\ \theta = \frac{k\lambda}{D} + 4\varepsilon\ sin\ \theta \quad (4)$$

The slope and intercept from the linear fit of the W- H plot is illustrated in Figure.3.3 which provides the value of micro strain and crystallite size of the prepared La_2CoMnO_6 respectively and summarized in Table 3.2. The appreciable straight line in the W – H plot illustrates the uniform distribution of crystallite size and micro strain [82–84].

Table 3.1: Structural and refinement parameters obtained from the Rietveld pattern of La_2CoMnO_6 double perovskites.

Sample name	**Unit cell parameters**		**V ($Å^3$)**	**Tolerance factor (t)**	**Refinement Parameters**	
La_2CoMnO_6	a (Å)	5.527	234.933	0.90	R_p	7.49
	b (Å)	5.470			R_{wp}	9.42
	c (Å)	7.769			χ^2	2.66
	β (deg)	89.892				

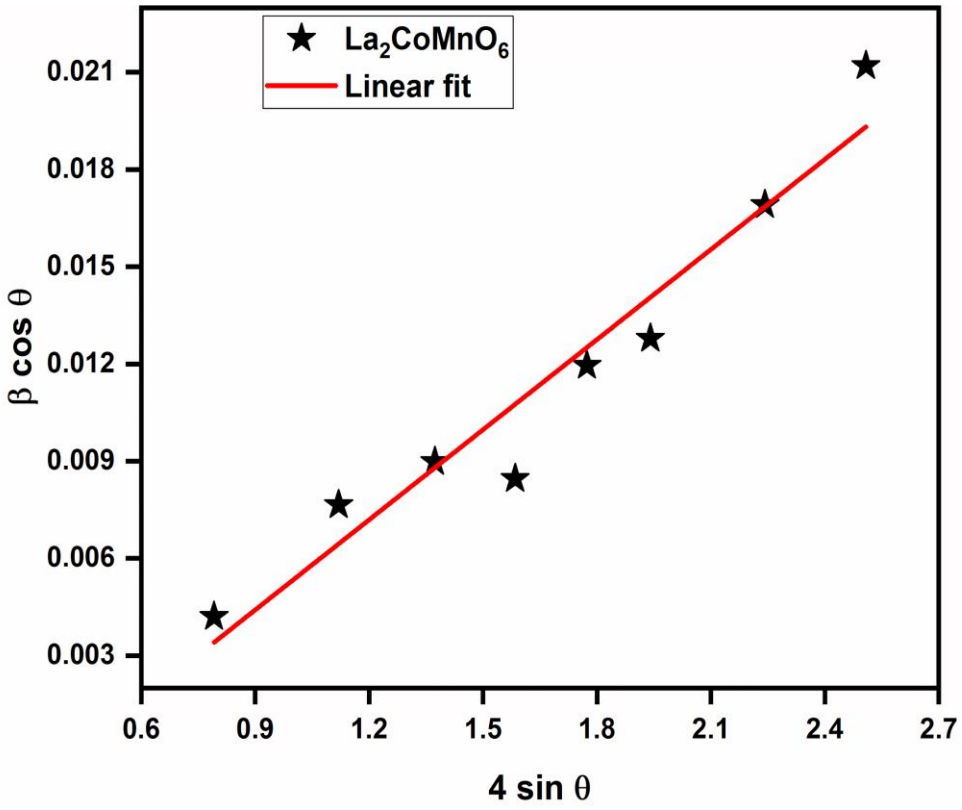

Figure. 3.3. W-H plot of La_2CoMnO_6 double perovskites.

Table 3.2: Crystallite size and micro strain calculated from W-H plot of La_2CoMnO_6 double perovskites.

Sample name	**Crystallite size (nm)**	**Micro strain**
La_2CoMnO_6	34.80	9.27×10^{-3}

Surface morphology of La_2CoMnO_6 double perovskites can be determined using field emission scanning electron microscopy. The particles exhibit a porous structure with an irregular shape, as

shown in Figure. 3.4 (a) [80]. The elemental composition of the prepared double perovskite is investigated using the EDAX spectra. The spectra depicted in Figure. 3.4 (b) exhibit peaks corresponding to La, Co, Mn, and O, and its atomic weight percentage is tabulated in the inset table, thus confirming the formation of La_2CoMnO_6 double perovskites.

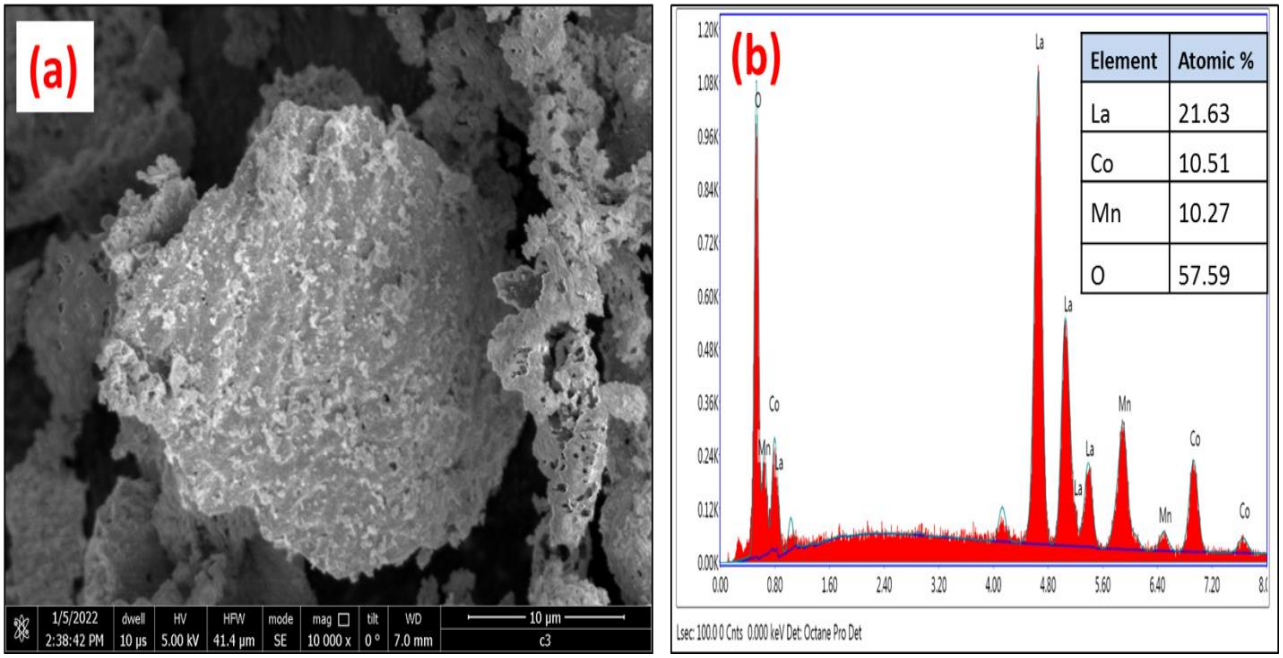

Figure. 3.4 (a, b). FE-SEM and EDAX spectra of La_2CoMnO_6 double perovskites,Inset table: atomic percentage of La, Co, Mn and O in La_2CoMnO_6 double perovskites.

3.2.2 BET - surface area analysis

Surface area and pore diameter of the prepared La_2CoMnO_6 compound are analyzed by using N_2 adsorption-desorption isotherms at 200°C for 3h. It follows a type IV isotherm in the pressure range of 0 to 1, indicating large pore size mesopores. The BET surface area sample is about 1.988 m^2/g. The BJH method is employed for the determination of pore size distributions, and we obtained the pore diameter as 12.52 nm. This higher value of pore diameter produces the feasibility of intercalation of ions

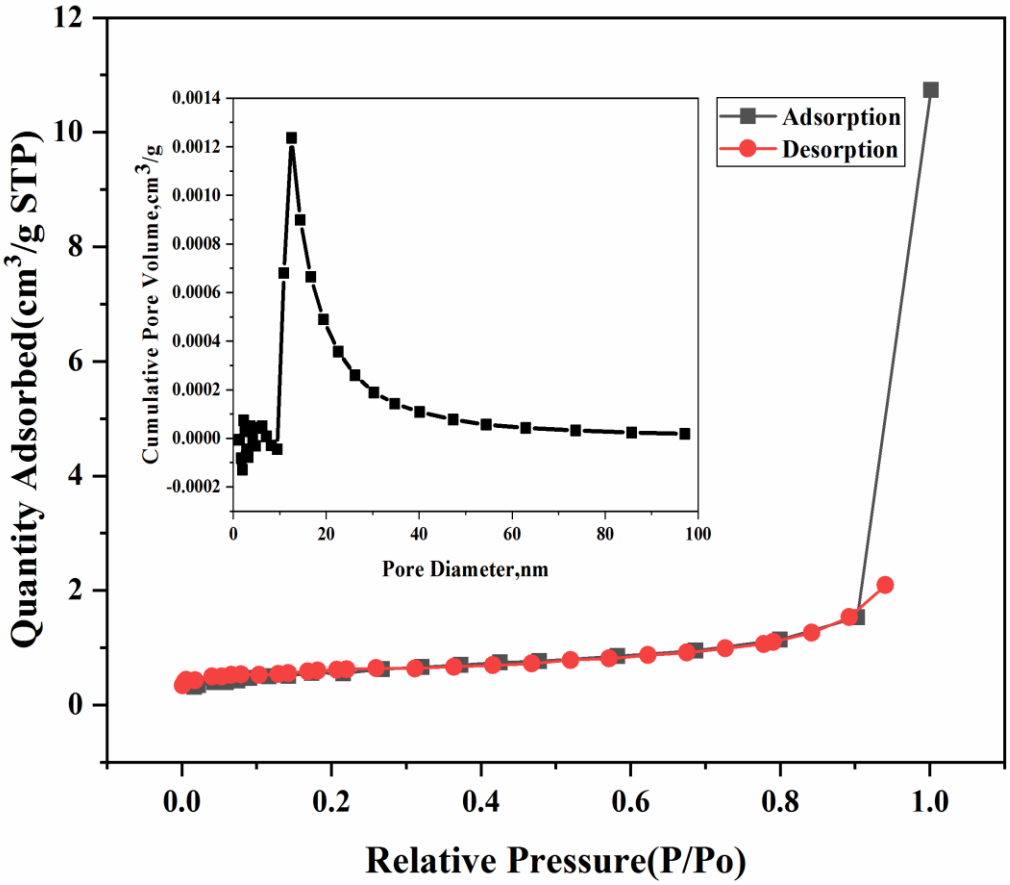

Figure. 3.5. BET analysis of La_2CoMnO_6 and inset graph represent the pore size distribution using BJH.

3.2.3 Surface Chemical Composition and Oxidation States

The local electronic structure and oxidation states of all elements present on the sample surface can be determined from the XPS spectra. Figure.3.6 illustrates the survey spectra of La_2CoMnO_6 double perovskites, which exhibit the peaks corresponds to La, Co, Mn and O. There exist no other impurity peaks in the survey spectra, other than the C 1s peak at 285.03 eV, which is utilized for the calibration of binding energies [85]. Hence, the XPS spectra support the EDAX results by identifying the appearance of La, Mn, Co, and O elements in the synthesized material. Figure.3. 7 (a) indicates the core level XPS spectra of La 3d states, which have two main peaks with binding energies centered at 833.59 and 850.39 eV which attributes to La $3d_{5/2}$ and La $3d_{3/2}$, and their respective satellite peaks are identified at 837.55 eV and 854.34 eV. The core-level spectra of Co

2p shown in Figure. 3.7 (b) has two peaks at the binding energies 779.62 eV and 795.31 eV and are assigned to 2p $_{3/2}$ and 2p $_{1/2}$ states respectively and the spin-orbit difference between these two preceding doublets is about 15 eV. On deconvoluting, the peaks at 779.37 eV and 794.92 eV correspond to Co $^{3+}$ while the peaks around 780.74 eV and 796.45 eV are assigned to Co $^{2+}$ oxidation states. As shown in Figure.3.7 (c), the Mn 2p spectra exhibit two prominent peaks at 641.81 eV and 653.53 eV, which arise from spin-orbit coupling and are attributed respectively to Mn 2p $_{3/2}$ and Mn 2p $_{1/2}$ states. The spin-orbit splitting energy between these doublets is about 12 eV which validates the presence of Mn^{3+} and Mn^{4+} oxidation states. The peak at 641.86 eV is deconvoluted into two peaks centered on 641.57 eV and 643.39 eV while the peak at 653.43 eV can be split into two components centered at 653.17 eV and 655.32 eV which match well with the binding energy of Mn^{3+} and Mn^{4+} oxidation state correspondingly [86]. Thus, the existence of mixed valence states of Mn and Co is verified from the XPS spectra. Figure.3.7 (d**)** shows the O1s spectra in which the peak at 528 eV represents the metal-oxygen bond while the peak centered around 530 eV is assigned to hydroxyl groups that exist on the surface of La_2CoMnO_6 as identified from the FTIR result.

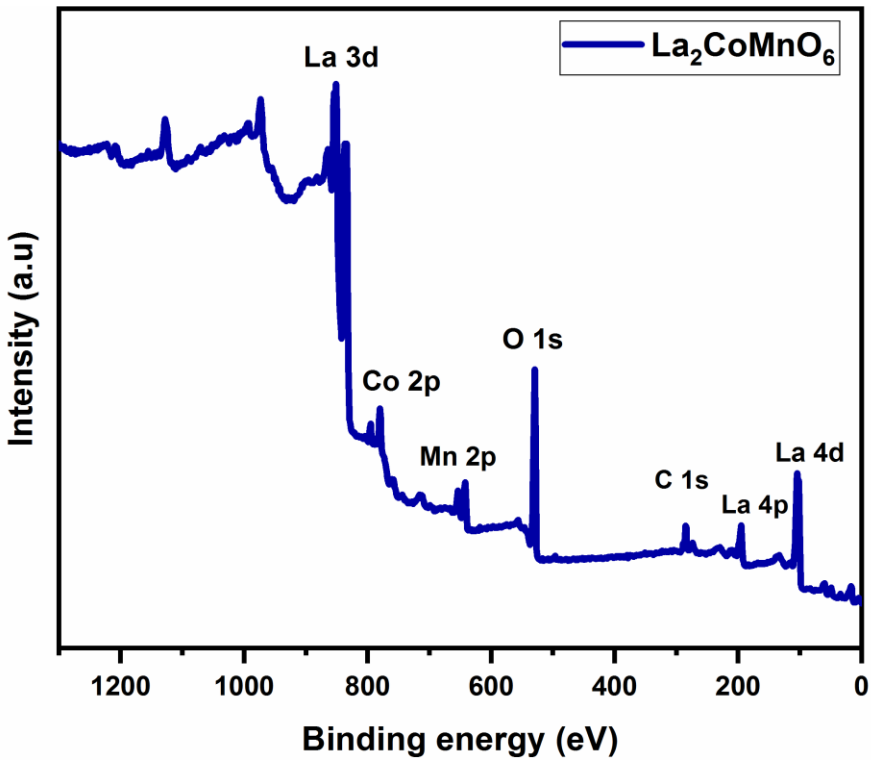

Figure.3.6. XPS survey spectrum of La_2CoMnO_6 double perovskites.

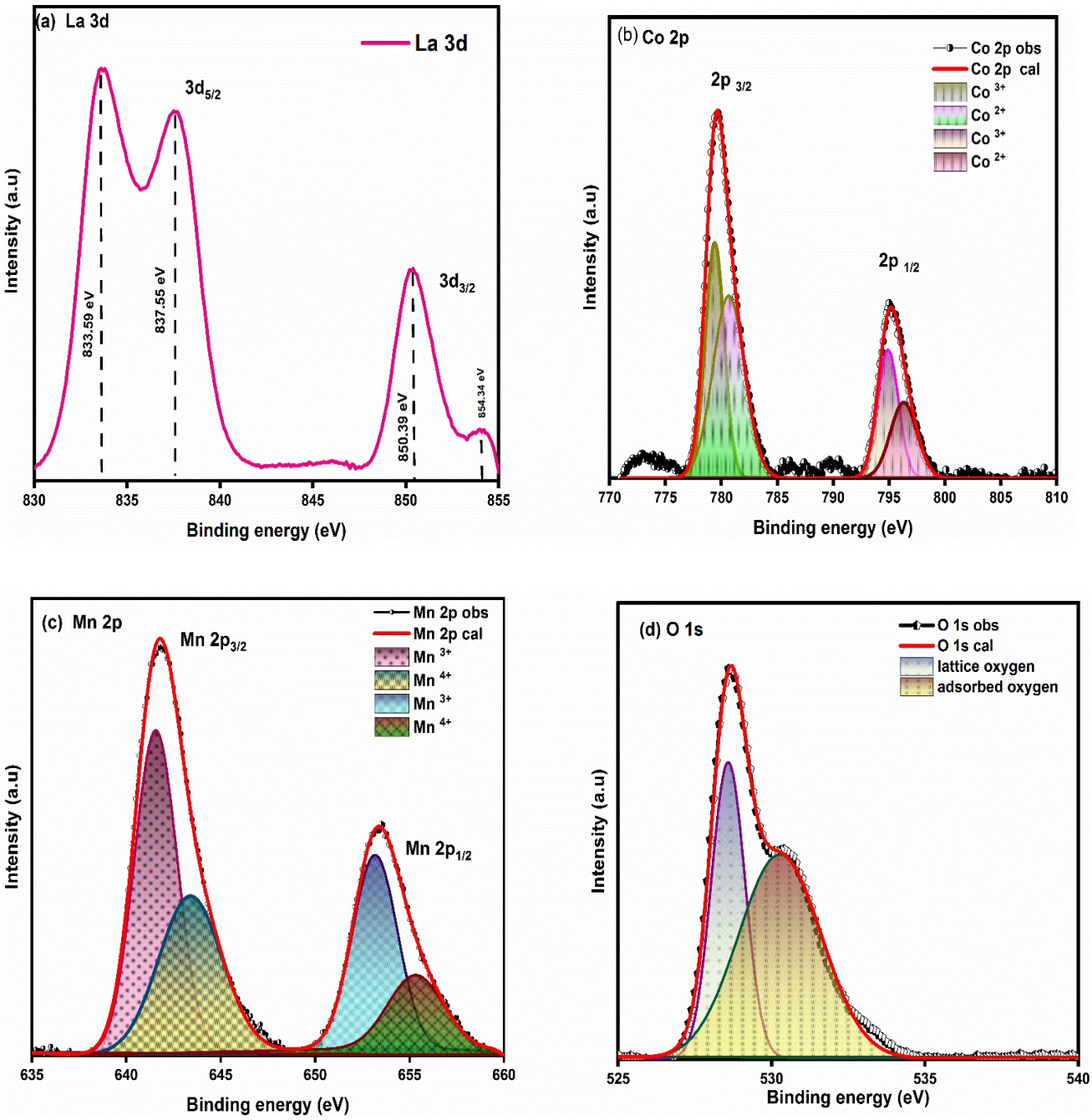

Figure. 3.7 (a-d). Core level XPS spectra of La, Co, Mn, and O.

3.2.4 Vibrational studies

The non-destructive vibrational spectroscopic methods are found to be very useful in evaluating the available surface functional groups and modes of vibration in the prepared sample. Among

these, Raman spectroscopy is an efficient tool for determining the local structure of various phases in the synthesized double perovskite. By examining the symmetries and Wyckoff positions in La_2CoMnO_6 possessing monoclinic geometry with $P2_1/n$ space group, the irreducible representation of the C_{2h} factor group holds 57 optical active modes. Table 3.3 gives the normal vibrational bands of La_2CoMnO_6 at the Brillouin zone center. As a result, two types of Raman active modes for La_2CoMnO_6 are observed i) A_g and ii) B_g as shown in Figure. 3.8.

Table 3.3: Normal vibrational modes of La_2CoMnO_6 at the Brillouin zone centre.

Number	**Active mode type**	**Centre of Brillouin zone (Γ)**
24	Raman active mode	$\Gamma_{Raman} = 12\ A_g \oplus 12\ B_g$
33	IR-active mode	$\Gamma_{IR} = 17\ A_u \oplus 16\ B_u$
3	Acoustic mode	$\Gamma_{acoustic} = A_u \oplus B_u$

From the expected 24 modes, the current work has identified only 3 modes of vibration. It is because of the thermal broadening and/or degeneracy in Raman modes that the other modes may get suppressed/merged [97]. Signature vibrational bands in La_2CoMnO_6 have been observed, in the 500 –700 cm^{-1} range, consisting of both stretching and bending motions of the Co- and Mn-centered octahedra [87]. More precisely, the spectrum is dominated by two bands. One is the most intense peak at 654 cm^{-1}, which represents the symmetric stretching vibrations of MnO_6 and CoO_6 octahedra, and second one, the broad reflection at 490 - 520 cm^{-1}, is readily assigned as inter mixed anti-stretching and bending vibrations [88–90]. The line at 654 cm^{-1} is viewed as the highest energy phonon mode with A_g symmetry. These modes not only predict the B-site ordering of the monoclinic structure but also the lattice

distortions [91]. In addition to characteristic modes, a broad multiphonon band between 1288 -1310 cm^{-1} is observed, which is considered to be the higher order overtone of the breathing mode and twice of the breathing mode [92].

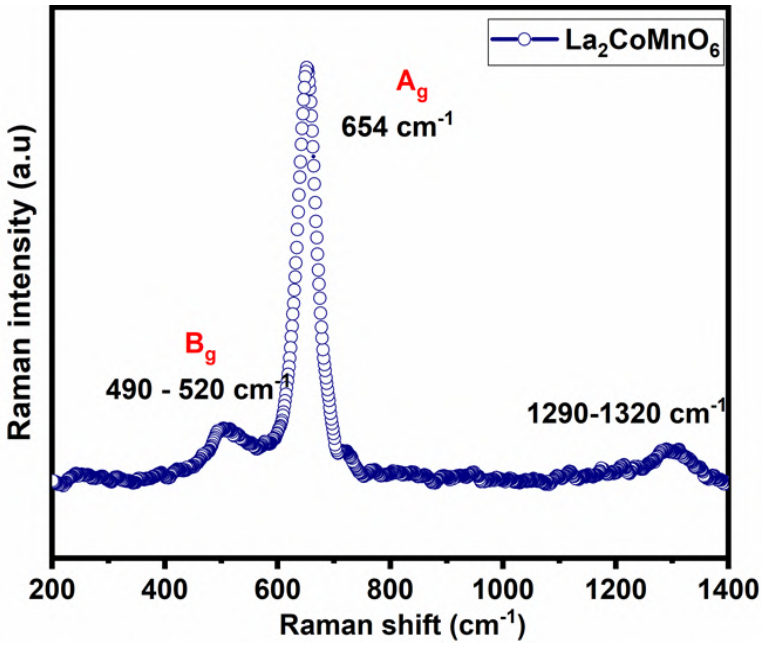

Figure. 3.8. Raman spectrum of La_2CoMnO_6.

The FTIR spectrum of La_2CoMnO_6 is evaluated in a wide range of wavenumbers, from 0 - 400 cm^{-1} and 400 - 3500 cm^{-1}, shown in Figure. 3.9 (a, b). As per literature, lower symmetry of the sample can be validated from the splitting of IR bands at a lower wavenumber. FTIR spectra of perovskite exhibits characteristic absorption bands in the range of 400 to 850 cm^{-1} [93]. The bands obtained between 200 -350 cm^{-1} are attributed to the bending modes of free octahedra [94]. Moreover, external modes with lowest energy are ascribed below 200 cm^{-1}. The appearance of a strong and intense band in La_2CoMnO_6 below 650 cm^{-1}, confirms the formation of the perovskite phase, as it is the fingerprint mode of vibration of rare-earth based double perovskite. Generally, bands between 500 – 535 cm^{-1} attributes to the Mn - O stretching vibration in octahedra [95]. Furthermore, the most intense peak band is observed around 560 cm^{-1} corresponding to the anharmonic asymmetric stretched mode of MnO_6 [96], which in turn confirms the formation of MnO_6 octahedra [97]. The splitting of spectral lines in the lower energy band in the range 530 cm^{-1} to 400 cm^{-1} can be attributed to the MnO_6

polyhedra deformational mode. A small deformation between 1000 -1050 cm^{-1} in the spectra can be related to the symmetric stretching vibration of MnO_6 octahedra. [98]. An intense peak located at 472 cm^{-1} evolved due to the symmetric stretching of MnO_6 about Mn - O bond length [99]. The mid-infrared (650 cm^{-1} – 550 cm^{-1}) bands normally appear in lanthanum – manganese perovskites due to the internal motion of manganese ions into the octahedra caused by the symmetric Mn – O – Mn stretching vibrations in MnO_6 [100]. According to reports, the stretching mode is associated with changes in Metal – Oxygen - Metal (Mn – O – Mn) bond length, whereas the bending modes are associated with changes in Mn – O – Mn bond angle [90]. Presence of such modes explains the perovskite structure of La_2CoMnO_6, which supports the XRD findings.

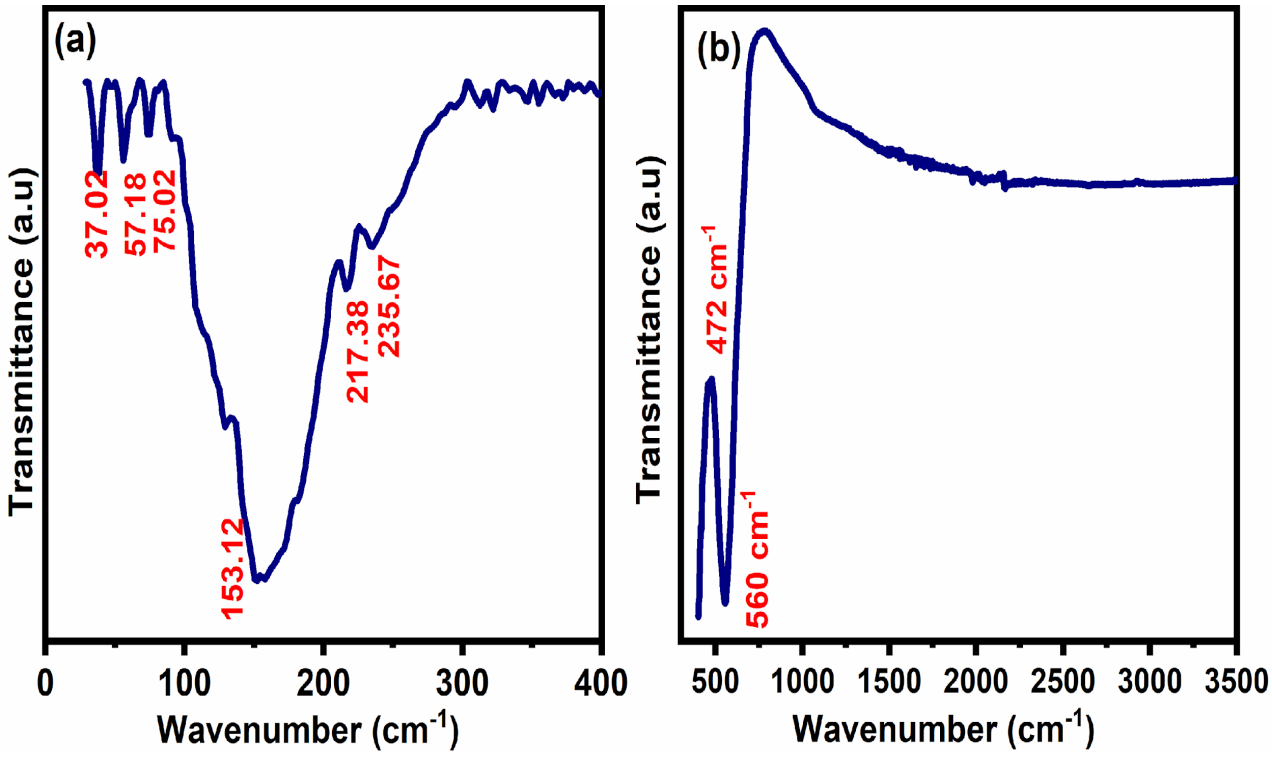

Figure. 3.9 (a). FAR-IR and (b) FTIR spectrum of La_2CoMnO_6.

Table 3.4: Wavenumber, active symmetry and vibrational modes of La_2CoMnO_6.

Wavenumber (cm^{-1})	Active symmetry	Reason
490-520	B_g	Symmetric stretching vibrations of MnO_6 octahedra (breathing mode)
654	A_g	Jahn–Teller stretching mode-antisymmetric stretching vibrations

3.2.5 Optical studies

Figure. 3.10 (a) illustrates the absorption spectrum of the La_2CoMnO_6. The valence band and conduction band are Co/Mn t_{2g}, O 2p and Co/Mn e_g orbital respectively [100]. The energy bandgap (E_g) of La_2CoMnO_6 is calculated using the formula reported by Tauc, Mott, and Dav

$$(\alpha h\vartheta)^{1/n} = A(h\vartheta - E_g) \quad (5)$$

where α = coefficient of absorption, $h\vartheta$ = incident energy, A = proportionality constant and n is an index with values 2, 3, 1/2, 3/2, corresponding to direct allowed transition, indirect allowed transition, indirect forbidden transition and direct forbidden transition, respectively.

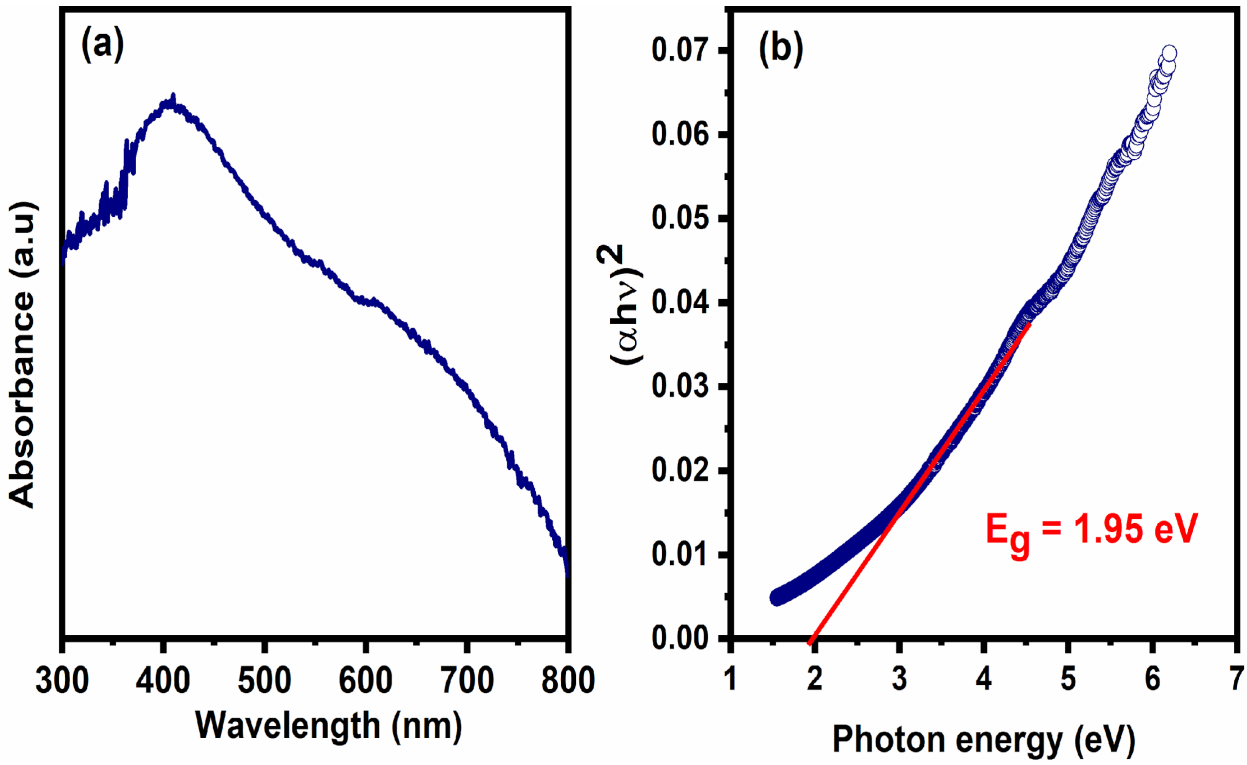

Figure. 3.10. (a) Absorbance spectrum and (b) Tauc plot of La_2CoMnO_6.

Usually, perovskites have direct allowed transition, hence we choose n = 1/2. Bandgap (E_g = 1.95 eV) is determined from the Tauc plot, as in Figure. 3.10 (b) by extrapolating the tangent line on $(\alpha h\vartheta)^2$ to x – axis. The energy band gap observed in the sample indicates immense applications in the field of photovoltaic devices and light harvesting [100].

3.3 Electrochemical performance

The electrochemical performance of the electrodes is analyzed with the help of a standard three - electrode system containing a Pt wire as a counter electrode and an Ag/AgCl (sat. KCl) as a reference electrode. The working electrode is manufactured by making slurry with active material (La_2CoMnO_6), acetyl black, and polytetrafluoroethylene (PTFE) according to a mass ratio of 85: 10: 5 in N – methyl – 2 - pyrrolidone (NMP). The mixture is coated evenly over the stainless-steel substrate. All the electrochemical measurements are carried out in a 1M Na_2SO_4 electrolyte medium.

The supercapacitor performance of the as-prepared La_2CoMnO_6 is studied by CV in 1M Na_2SO_4 electrolyte over a potential range of -0.2 to 0.8 V. The CV plot of the La_2CoMnO_6 at different scan rates (10-100 mV s^{-1}) are given in Figure. 3.11.

The specific capacitance of the La_2CoMnO_6 is calculated as per the relation,

$$Cs = \frac{Idv}{2mVdv} \quad (6)$$

Where, Idv denotes the area under the CV curve, m the mass of active material loaded, V the scan rate, and dv is the working operational window. The CV curves of electrode material remained symmetrical at high scanning rates. The CV calculations reveal that the developed sample provides a specific capacitance of 14 mF g^{-1}. From these calculations, it is found that the sample possesses a specific capacitance of 14 mFg^{-1}. The shape of the curve reveals that the material has an electrical double layer capacitance (EDLC) behaviour with a quasi-reversibility, indicating that the material has higher charge transfer characteristics and good multiplying power. The electrode material shows this behaviour because of its higher specific surface area and enlarged pore structure. These factors produce a faster diffusion of electrolyte ions, facilitating the super capacitive behaviour.

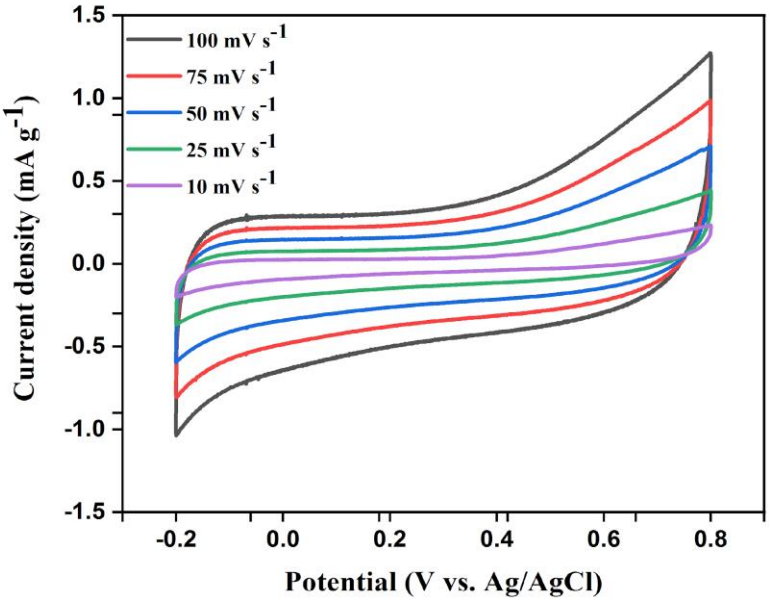

Figure. 3.11. CV curve of La_2CoMnO_6 at different scan rate.

The specific capacitance and electrochemical stability of the composite are also studied using the GCD curve given in Figure. 3.12. The GCD curves obtained at different currents having potential range as the CV curve is given in Figure. 3.12. The specific capacitance of the material is quantified from the equation,

$$Cs = \frac{I\Delta t}{m\Delta V} \quad (7)$$

here, I denote discharge current, Δt the discharge time, m the mass loaded, and ΔV the potential window.

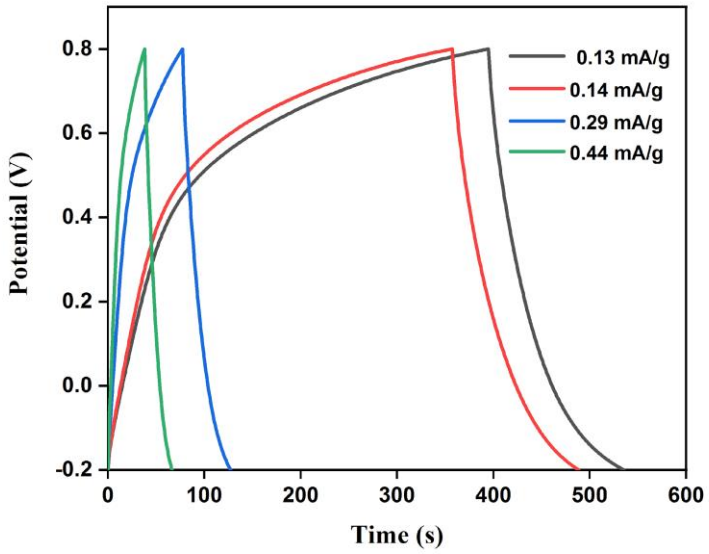

Figure. 3.12. GCD curve at different current densities.

According to the above equation, the specific capacitance of the La_2CoMnO_6 determined from the GCD curve is 19.4, 14.9, and 13 mF g^{-1} at a current density of 0.14, 0.29, and 0.44 mA g^{-1}, respectively given in Table 3.5. The specific capacitance of La_2CoMnO_6 material is due to its higher aspect ratio, which produces the feasibility of electrolyte ions to penetrate easily and make complete contact with the electrode material, introducing higher supercapacitor performance of electrodes. The structure of La_2CoMnO_6 consists of an octahedron site, producing a continuous channel for rapid migration of electrode charges, improving the electrode material conductivity and thereby increasing the utilization efficiency of the electrode [81]. There exists a more ordered arrangement of A-site and B-

site cations in double perovskites. This ordering of cations produces an improved diffusivity of oxygen in perovskite oxides, thereby increasing the supercapacitor performance. Cation ordering in La_2CoMnO_6 creates oxygen vacancies, and higher vacancies introducing large spaces for oxygen ion intercalation from electrolyte solution, thereby producing an improvement in supercapacitor performance. These properties are due to the inherent efficiency of double perovskites to tolerate the A-cation deficiencies [101]. The charge storage mechanism in La_2CoMnO_6 is given as

$$(A)_{Surface} + Na^+ + e^- \longleftrightarrow (A - Na^+)_{surface}$$

$$(BO)_{surface} + Na^{++} e^- \longleftrightarrow (BO - Na^+)_{surface}$$

Figure 3.13 represents the Nyquist plot of the desired material. The plots are fitted with the equivalent electrical circuit using the Z-fit software, and the corresponding parameters are analyzed. The evaluation of the fitted circuit shows that the La_2CoMnO_6 possesses lower R_e (2.12Ω) and R_{ct} (1.62Ω) values.

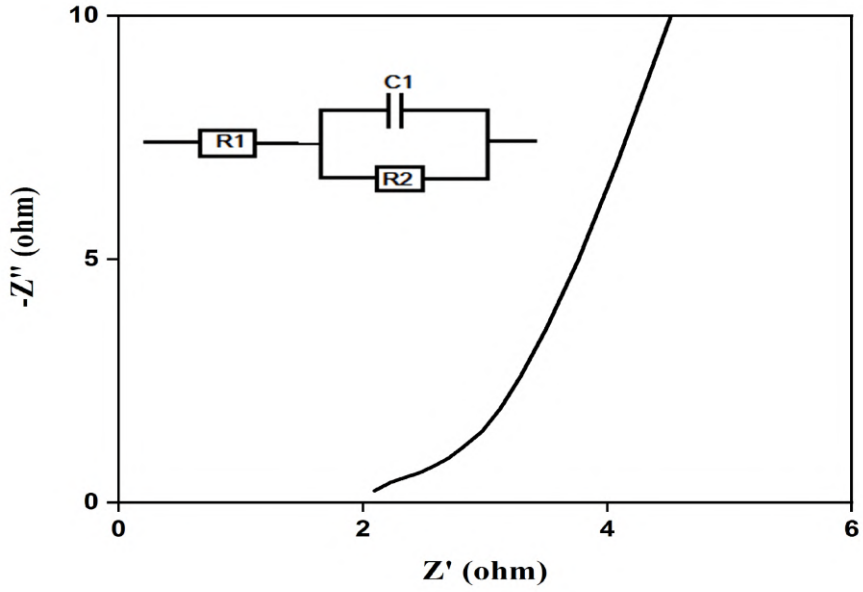

Figure. 3.13. Nyquist plot of La_2CoMnO_6

Table 3.5: Specific capacitance, energy density and power density.

Current density (mA g^{-1})	Specific capacitance (mF g^{-1})	Energy density (Wh kg^{-1})	Power density (W kg^{-1})
0.14	19.4	0.0027	0.0746
0.29	14.9	0.002	0.1492
0.44	13	0.0018	0.2238

Cyclic stability is an important parameter for a supercapacitor, which is depicted in Figure. 3.14. It confirms that 84 % coulombic efficiency is maintained even after 500 cycles in a three-electrode system.

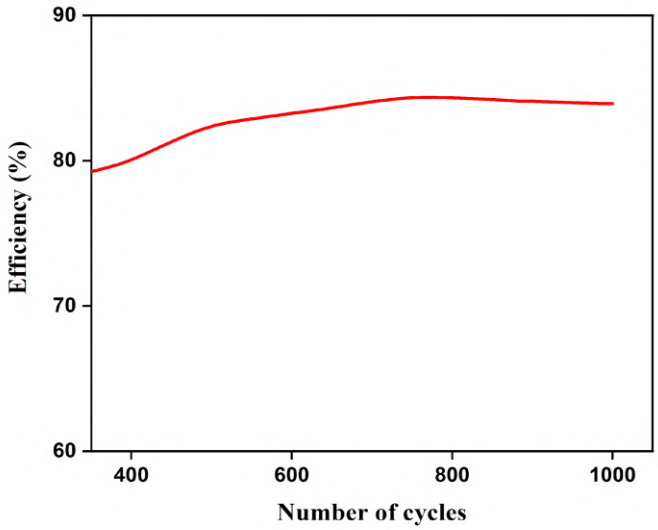

Figure. 3.14. Cyclic performance of La_2CoMnO_6 at a current density 0.29 mA g^{-1}.

Figure. 3.15 depicts a Ragone plot of the La_2CoMnO_6 derived from the GCD curve at various current densities. The specific energy density (E) and specific power density (P) are evaluated as

$$E = \frac{Cs\Delta V^2}{2\times 3.6} \quad (8)$$

$$P = \frac{E\times 3600}{t} \quad (9)$$

here, Cs represents the specific capacitance, ΔV the potential window, and t the discharge time.

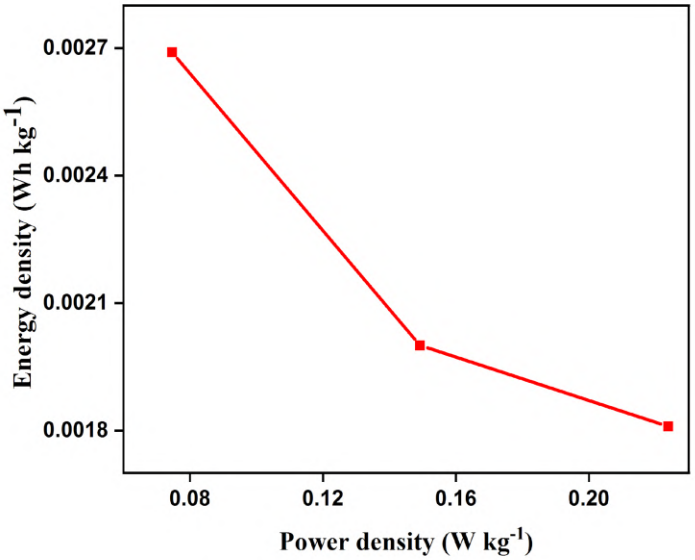

Figure. 3.15. Ragone plot of La_2CoMnO_6.

CHAPTER 4

CONCLUSION AND FUTURE SCOPE

4.1 Conclusion

La_2CoMnO_6 double perovskite were considered to be an outstanding candidate for the future generation memory gadgets due to their multifunctional properties. Herein, La_2CoMnO_6 was successfully synthesized using modified combustion method. The XRD pattern reveals the monoclinic structure with a space group of $P2_1/n$ and its crystallite size and micro strain were determined from the Williamson – Hall plot. Irregular shaped porous structures were observed from the FE-SEM images and the EDAX spectrum confirms the existence of elements La, Co, Mn and O. The existence of mixed valence states of Co and Mn were verified from the XPS spectra. The surface area of the prepared material was about 1.988 m^2/g. FTIR and Raman spectra confirm finger print mode vibration of rare-earth based double perovskite. The Raman active A_g and B_g modes respectively correspond to the Jahn – Teller stretching mode- antisymmetric stretching vibrations and symmetric stretching vibrations of the MnO_6 octahedra (breathing mode). In FTIR spectra, external modes with lowest energy are ascribed below 200 cm^{-1}, whereas the splitting of spectral region 530 cm^{-1} to 400 cm^{-1} is attributed to the deformational mode of MnO_6 polyhedra. The band gap were identified in between the Co/Mn t_{2g} and O 2p hybridization bands, and the Co/Mn e_g orbital, and is evaluated as 1.95 eV using Tauc plot. La_2CoMnO_6 nanoparticle-based electrode material shows 84 % cyclic stability after 500 cycles with 13 mF/g specific capacitance at a current density of 0.44 mA/g. The results revealed that the prepared electrode material efficiently worked as a superior electrode material among double perovskites.

4.2 Future Scope

Double perovskite manganite materials like La_2CoMnO_6 have received enormous interest due to its multifunctional properties like Curie temperature, magneto resistive effects, optical band gap etc. In this project work, pristine La_2CoMnO_6 were synthesized using modified combustion method and its structural, morphological, vibrational, optical and electrochemical performance were investigated in detail. In order to find an efficient supercapacitor, the electrochemical properties of La_2CoMnO_6 can be explored by doping various elements. With substitution for Mn, the properties such as structural, optical, electrochemical may be transformed immensely. The combination of La_2CoMnO_6 with other elements may give rise to a material with better properties. Also, it is expected that in future this compound be can synthesized using different methods like sol-gel method, hydrothermal method, co-precipitation method and its sintering temperature can be varied accordingly. Also it can be subjected for various applications like photo catalysis studies under UV/ sunlight, gas sensors and solar cells. Also, its magnetic properties can be explored. Since the coupling of multiple coexisting states in this perovskite manganite provides a playground for the creation of novel physical properties and device concepts, the nonlinear optical properties (NLO) of La_2CoMnO_6 double perovskite also can be analyzed which have not yet been explored so far.

References

1. S.D. Balgude, S.S. Barkade, S.P. Mardikar, Multifunctional Nanostructured Metal Oxides for Energy Harvesting and Storage Devices, CRC Press, (2020) 169– 194.
2. M.G. Walter, E.L. Warren, J.R. McKone, S.W. Boettcher, Q. Mi, E.A. Santori, N.S. Lewis, Solar water splitting cells, Chem. Rev., 110 (2010) 6446–6473.
3. B.E. Conway, Electrochemical Supercapacitors, Kluwer Academic/Plenum Publishers, New York, 1999.
4. P. Xie, W. Yuan, X. Liu, Y. Peng, Y. Yin, Y. Li, Z. Wu, Energy Storage Matter, 36 (2021) 56–76.
5. A. Muzaffar, M.B. Ahamed, K. Deshmukh, J. Thirumalai, Renew. Sustain. Energy Rev., 101 (2019) 123–145.
6. M.K. Khawaja, M.F. Khanfar, T. Oghlenian, W. Alnahar, Comput. Electr. Eng., 85 (2020) 106678.
7. D.P. Dubal, Y.P. Wu, R. Holze, ChemTexts, 2 (2016) 13.
8. B.K. Kim, S. Sy, A. Yu, J. Zhang, in: Handb. Clean Energy Syst., John Wiley & Sons, Ltd, Chichester, UK, (2015) 1–25.
9. N. Kularatna, in: Energy Storage Devices Electron. Syst., Elsevier, (2015) 1–28.
10. Juhan Lee, Volker Presser, Progress in Materials Science, 101 (2019) 46-89, 0079-6425
11. G.Z. Chen, Int. Mater. Rev., 62 (2017) 173–202.
12. B.E. Conway, in: Electrochem. Supercapacitors, Springer US, Boston, MA (1999) 105–124.
13. A. Burke, J. Power Sources, 91 (2000) 37–50.
14. D.P. Dubal, Y.P. Wu, R. Holze, ChemTexts, 2 (2016) 13.
15. M. Inagaki, M. Toyoda, Y. Soneda, T. Morishita, Carbon N. Y., 132 (2018) 104–140.
16. B.E. Conway, in: Electrochem. Supercapacitors, Springer US, Boston, MA, (1999) 221–257.
17. V. Augustyn, P. Simon, B. Dunn, Energy Environ. Sci., 7 (2014) 1597.
18. W. Zuo, R. Li, C. Zhou, Y. Li, J. Xia, J. Liu, Adv. Sci., 4 (2017) 1600539.
19. M. Winter, R.J. Brodd, What are batteries, fuel cells, and supercapacitors? Chem. Rev., 104 (2004) 4245–4269.

20. J. Lai, S. Levy and M. F. Rose, IEEE Aeros. Electron. Syst. Mag., 7 (1992) 14-19.

21. H. Douglas and P. Pillay, Proceedings of the 31st Annual Conference of IEEE Ind. Electron. Soc., (2005) 6-10.

22. N. G. Hingorani, IEEE Spectrum, 32, (1995) 41-48.

23. R.R. Salunkhe, J.J. Lin, V. Malgras, S.X. Dou, J.H, Kim and Y. Yamauchi, Nano Energy, 11 (2015) 211-218.

24. M. E. Glavin, P. K. W. Chan, S. Armstrong and W. G. Hurley, Proceedings of the 13th Power Electronics and Motion Control Conference, (2008) 1688-1695.

25. Y. Wang, J. Guo, T.F. Wang, J.F. Shao, D. Wang and Y.W. Yang, Nanomater.Basel, 5 (2015) 1667-1689.

26. L.B. Jiang, X.Z. Yuan, J. Liang, J. Zhang, H. Wang and G.M. Zeng, J. Power Sources, 331 (2016) 408-42.

27. D. Linzen, S. Buller, E. Karden and R. W. De Doncker, IEEE Trans. Ind. Appl., 41 (2005) 1135-1141.

28. D. Kiran, A. Palani, S. Muthukumar and V. Jayashankar, IEEE Trans. Energy Convers. 22 (2007) 539-540.

29. S. Muthukumar, S. Kakumanu, S. Sriram and V. Jayahankar, Proceedings of the IEEE International Conference on Electric Machine and Drives, (2005) 193-198.

30. D.P. Dubal, O. Ayyad, V. Ruiz, P. Gómez-Romero, J. Chem. Soc. Rev., 44 (2015) 1777–1790.

31. M. Meyyappan, J. Vac. Sci. Technol. A Vacuum, Surfaces, Film, 31 (2013) 050803.

32. Z. Jia, W. Lu, Y. Wang, Y. Liang, Y. Li, S. Feng, J. Electrochim. Acta. 159 (2015) 35–39.

33. C. Wang, F. Li, Y. Wang, H. Qu, X. Yi, Y. Lu, Y. Qiu, Z. Zou, B. Yu, Y. Luo, J. Alloys Compd., 634 (2015) 12–18.

34. C.C. Hu, J.C. Chen, K.H. Chang, J. Power Sources 221 (2013) 128–133.

35. J. Jiang, J. Liu, W. Zhou, J. Zhu, X. Huang, X. Qi, H. Zhang, T. Yu, J. Energy Environ. Sci., 4 (2011) 5000.

36. M.M. Sk, C.Y. Yue, K. Ghosh, R.K. Jena, J. Power Sources, 308 (2016) 121–140.

37. W.H. Low, P.S. Khiew, S.S. Lim, C.W. Siong, E.R. Ezeigwe, J. Alloys and Compd., 775 (2019) 1324–1356.

38. A.K. Yedluri, H.-J. Kim, RSC Adv., 9 (2019) 1115–1122.

39. A.J.C. Mary, A.C. Bose, Appl. Surf. Sci., 449 (2018) 105–112.

40. J. Li, D. Xiong, L. Wang, M.K.S. Hirbod, X. Li, J. Energy Chem., 37 (2019) 66–72.

41. Y. Lin, J. Wang, H. Yang, L. Wang, M. Cao, Mater. Lett., 207 (2017) 195–197.

42. L. Fang, F. Wang, T. Zhai, Y. Qiu, M. Lan, K. Huang, Q. Jing, Electrochim. Acta., 259 (2018) 552–558.

43. G.K. Veerasubramani, K. Krishnamoorthy, R. Sivaprakasam, S. J. Kim, Mater. Chem. Phys., 147 (2014) 836–842.

44. F.K. Butt, M. Tahir, C. Cao, F. Idrees, R. Ahmed, W.S. Khan, Z. Ali, N. Mahmood, M. Tanveer, A. Mahmood, I. Aslam, ACS Appl. Mater. Interfaces, 6 (2014) 13635 –13641.

45. S. Qiao, N. Huang, Y. Sun, J. Zhang, Y. Zhang, Z. Gao, J. Alloys Compd., 775 (2019)1109–1116.

46. A. A. Emery and C. Wolverton, Sci. Data, 4 (2017)170153.

47. G. Ja´come-Acatitla, M. A´lvarez-Lemus, R. Lo´pez-Gonza´lez,C. Garcı´a-Mendoza, A. Sa´nchez-Lo´pez and D. Herna´ndez-Acosta, J. Photochem. Photobiol, A, 390 (2020) 11233.

48. J. T. Mefford, W. G. Hardin, S. Dai, K. P. Johnston and K. J. Stevenson, Nat. Mater., 13 (2014) 726–732.

49. R. X. Silva, A.S. Menezes, R. M. Almeida, R. L. Moreira, R. Paniago, X. Marti, H. Reichlova, M. Marysko, M. V. S. Rezende, C. W.A.Paschoal, J. Alloys Compd., 661 (2016) 541-552.

50. J. K. Murthy and A. Venimadhav, J. Appl. Phys., 111 (2012) 024102.

51. P. L. C. Filho, P. Barrozzo, D. A. Landinez- Teller, R. F. Jardim, W. M. Azevedo, J. A. Aguiar, J. Supercond. Nov. Magn., 26 (2013) 2521-2524.

52. R. X. Silva, R. L. Moreira, R. M. Almeid, R. Paniago, C. W. A. Paschoal, J. Appl. Phys., (2015).

53. N. M. Yousif, N. Makram, L. A. Wahab, J. Sol-Gel Sci. Technol., 98 (2021) 238-251.

54. L. Guo, Y. Bai, C. Huang, and W. Ma, J. Appl. Phys., 124 (2018) 065103.

55. D. Yang, T. Yang, Y. Chen, Y. Liang, and Y. Liu, J. Mater. Sci., 54 (2019) 6027-6037.

56. J. Fu, H. Zhao, J. Wang, Y. Shen, and M. Liu, Int. J. Miner. Metall., 25 (2018) 950.

57. Z. Meng, J. Xu, P. Yu, X. Hu, Y. Wu, Q. Zhang, Y. Li, L. Qiao, Y. Zeng, H. Tian, Chem. Eng. J., 400 (2020) 125966.

58. J. Singh and A. Kumar, Int. J. Miner. Metall., 27 (2020) 987.

59. J. James, R. Jose, Asha M. John, J. Koshy, US Patent No. 6,761,866, July 13 (2004).

60. J. James, R. Jose, Asha M. John, J. Koshy, US Patent No. 6,835,367, December 2 (2004).

61. B.D. Cullity, Elements of X- Rays Diffraction, 3rd Edition, prentice hall, USA, (2001).

62. T. Pradeep, Nano: The Essentials, Understanding Nanoscience and Nanotechnology. US: McGraw-Hill Education, (2007).

63. O.C. Wells, Scanning Electron Microscopy, McGraw Hill, Inc. USA, (1974).

64. D. C. Bell, A. J. Garratt-Reed, Energy Dispersive X-ray Analysis in the Electron Microscope. Microscope Handbooks Series. New York: BIOS Scientific, (2003), 160.

65. K.D. Moulder, J. F., Stickel, W. F., Sobol, P. E., Bomben, Handbook of X-ray Photoelectron Spectroscopy, J. Chastain, Perkin-Elemer Corp., Minnesot, (1979).

66. S. Hüfner, Photoelectron Spectroscopy, Principles and Applications, 2nd edition, Springer-Verlag, Germany, (1995).

67. J. Rouquerol, F. Rouquerol, K. S. W. Sing, P. Llewellyn, G. Maurin. Adsorption by Powders and Porous Solids: Principles, Methodology and Applications, Academic Press (2014).

68. D.J. Gardiner, Practical Raman Spectroscopy, Springer-Verlag, (1989).

69. Kaufmann, E. N. *Characterization of Materials*, 2 *Volume Set* ISBN: 0-471-268828, 9780471268826 (Wiley- Interscience, 2003).

70. Smith, B. C. *Fundamentals of Fourier Transform Infrared Spectroscopy, Second Edition* 2nd ed. ISBN: 1420069292, 9781420069297, (2005).

71. Baharudheen S. Hameed, Anil K. Suresh, Chromatography as an efficient technique for the separation of diversified nanoparticles, Nanomaterials in chromatography, (2018).

72. Reserved, Mettlet-Toledo International Inc. All rights. "Spectroscopy Applications and Fundamentals". www.m.com. Retrieved 10 July (2018).

73. https://www.slideshare.net/mariomsS7/uvvis-spectrpscopy [im].

74. Counbia University Intensive Seminars In Modern Chemistry, Experiment 7 IR Spectroscopy.

75. A. Bard, L. Faulkner, Electrochemical Methods: Fundamentals and Applications, 2nd edition, John Wiley & Sons, Inc, (2001) 864.

76. B. E. Conway, in: Electrochem. Supercapacitors, Springer US, Boston, MA, (1999) 105–124.

77. M. E. Orazem, B. Tribollet, Preliminary Graphical Methods in: Electrochemical Impedance Spectroscopy, A John Wiley & Sons, Inc., New Jersey, (2008) 333.

78. R.I. Dass, J.B. Goodenough, Phys. Rev. B - Condens. Matter Mater. Phys., 67 (2003) 144011–144019

79. J.K. Murthy, A. Venimadhav, J. Appl. Phys., 111 (2012) 1123-1145

80. Z. Meng, J. Xu, P. Yu, X. Hu, Y. Wu, Q. Zhang, Y. Li, L. Qiao, Y. Zeng, H. Tian, Chem. Eng. J., 400 (2020).

81. J. Fu, H. Yan Zhao, J. run Wang, Y. Shen, M. Liu, Int. J. Miner. Metall. Mater., 25 (2018) 950–956.

82. N.M. Yousif, N. Makram, L.A. Wahab, J. Sol-Gel Sci. Technol., 98 (2021) 238–251.

83. R.X. Silva, A.S. De Menezes, R.M. Almeida, R.L. Moreira, R. Paniago, X. Marti, H. Reichlova, M. Maryško, M.V.D.S. Rezende, C.W.A. Paschoal, J. Alloys Compd., 661 (2016) 541–552.

84. N.S. Gonçalves, J.A. Carvalho, Z.M. Lima, J.M. Sasaki, Mater. Lett., 72 (2012) 36–38.

85. A.C. Ferrel-Álvarez, M.A. Domínguez-Crespo, H. Cong, A.M. Torres-Huerta, S.B. Brachetti-Sibaja, W. De La Cruz, J. Alloys Compd., 735 (2018) 1750–1758.

86. J. Krishna Murthy, A. Venimadhav, J. Appl. Phys., 113 (2013) 1–6.

87. T.I. Milenov, P.M. Rafailov, I. Urcelay-Olabarria, E. Ressouche, J.L. García-Muñoz, V. Skumryev, M.M. Gospodinov, Mater. Res. Bull.. 47 (2012) 4001–4005.

88. M.P. Reddy, X.B. Zhou, L. Jing, Q. Huang, Mater. Lett., 132 (2014) 55–58.

89. M.A. Magray, M. Ikram, J. Mater. Sci. Mater. Electron., 6 (2019).

90. N.M. Yousif, materials, (2021) 238–251.

91. C. Meyer, S. Hühn, M. Jungbauer, S. Merten, B. Damaschke, K. Samwer, V. Moshnyag, J. Raman Spectrosc., 48 (2017) 46–52.

92. S.C. Lal, A. Rajan, G. Subodh, Mater. Today Proc., 4 (2017) 4396–4402.

93. A. Rajan, G. Subodh, Ceram. Int., 46 (2020) 25683–25690.

94. O. Carp, L. Patron, A. Ianculescu, J. Pasuk, R. Olar, J. Alloys Compd., 351 (2003) 314-

318.

95. G. Pecchi, C. Campos, O. Peña, Mater. Res. Bull., 44 (2009) 846–853.

96. S. Das, T. Paul, S. Maiti, K.K. Chattopadhyay, Mater. Lett., 267 (2020) 127501.

97. A. Dutta, T.P. Sinha, Integr. Ferroelectr., 116 (2010) 41–50.

98. M.H. Habibi, V. Mosavi, J. Mater. Sci. Mater. Electron., 28 (2017) 8473–8479.

99. A. Machocki, T. Ioannides, B. Stasinska, W. Gac, G. Avgouropoulos, D. Delimaris, W. Grzegorczyk, S. Pasieczna, J. Catal., 227 (2004) 282–296.

100. F. Liu, Y. Gao, H. Chang, Y. Liu, Y. Yun, J. Magn. Magn. Mater. 435 (2017) 217–222.

101. Z. Xu, Y. Liu, W. Zhou, M.O. Tade, Z. Shao, ACS Appl. Mater. Interfaces. 10 (2018) 9415–9423.